Optical Sensors for Mechanomyography and Tissue Chromophores

Lund Institute of Technology

Div. of Atomic Physics

Bachelor Thesis

Emil Ljungberg

Supervisors: Prof. Lars Engström and Dr. Oliver Reich*

Examiner: Hans Lundberg

* Institute for Physical Chemistry, Potsdam University

December 7, 2013

Abstract

The mechanomyogram (MMG) is a mechanical oscillations observable on the surface of the skin as a muscle contracts. Measurement of the MMG utilizing contact sensors with a weight greater than 6 g has proved to interfere with the measurement. Use of optical displacement sensors without direct contact to the skin would remove this deficiency. A Michelson interferometer, an intensity shift set-up and a configuration able of measuring both MMG and tissue oxygenation dynamics simultaneously were all evaluated in regard to their precision, easy of use and efficacy. The results were analysed using the fast Fourier transform (FFT) and the continuous wavelet transform (CWT)

A regular Michelson interferometer proved to be unsuited for measuring oscillations with an amplitude greater than $\lambda/4$. Demodulation of signals exceeding this limit requires cumbersome analysis methods that would not be practically feasible in a clinical set-up.

By measuring the light reflected from an oscillating target, a second simpler set-up was able to measure the frequency and amplitude of a tuning fork with high precision. Measurements on biceps bracii was performed but no clear results were found.

A set-up combining MMG and tissue chromophores was realized with three optical fibres attached to the skin. The haemoglobin oxygenation dynamics was successfully measured during contraction and relaxation of the biceps brachii but no MMG signal could be deduced.

The outcome of this thesis suggest that further research is required to investigate the possibility of designing a set-up able to measure both MMG and haemoglobin oxygenation dynamics with high precision. This would enable a detailed study of muscle dynamics which have not been done before.

Contents

Preface

This paper is the written report of a bachelor thesis at Lund University with the experimental part completed at the institute for physical chemistry at the University of Potsdam. The report will focus on the theoretical background of the experimental work, the practical implementation of the measurement procedures and, of course, the results. The project was initiated through a collaboration between the department for sports medicine and the institute for physical chemistry at Potsdam University. This bachelor thesis is a first evaluation of possible future measurement methods.

The project was supervised by Dr. Oliver Reich with additional help from Marvin Münzberg, at the institute for physical chemistry at Potsdam University. The outline of the project was presented by Dr. Reich and my initial contribution was to perform a thorough literature search of previous research in the field as well as producing computer simulations of the proposed experiments before the practical work begun. Once the lab work commenced my main tasks included building the experimental set-ups in the lab, writing LabView programs, and performing measurements. The post-experimental part consisted of implementation of a python script for the continuous wavelet transform and maintaining contact with the department for sports medicine and the department for mathematics to discuss the validity of our results. This cross departmental communication is essential in this type of interdisciplinary research and proved to be invaluable in the medical and mathematical interpretation of our results.

Readers of this report are assumed to have the knowledge equivalent to a bachelors degree in physics or similar field. Basic understanding of electromagnetic waves, Fourier analysis, electronics and optics are required to get the most out of this report.

Populärvetenskaplig sammanfattning

Kirurgen står redo när patienten sakta faller in i en djupsömn av narkosen. För att garantera att patienten sover tillräckligt djupt skickar en apparat små elektriska impulser till en muskel i patientens pekfinger. Läkaren studerar hur muskeln i fingret reagerar och har där ett mått på vilket tillstånd av medvetslöshet patienten befinner sig i. Men hur mäter man reaktionen av den elektriska impulsen? Och vad är det man mäter?

Mekanomyogram (MMG) är studien av de mekaniska vibrationer som skapas när muskelfibrer kontraherar. Vibrationerna är ett mått på hur muskeln reagerar på de elektriska impulserna från nerver, eller i läkarens fall, den elektriska stimulansen. Vanliga metoder för att studera MMG är accelerometerar eller konventionella mikrofoner som monteras på muskeln man vill studera. Nackdelen med att fästa sensorn på mätobjektet är att man riskerar att påverka mätningen. En vardaglig analogi är när man spelar gitarr. Om du slår ann gitarrsträngen och sen sätter ett finger lätt på den vibrerande strängen kommer vibrationen dels dämpas men frekvens kan även ändras. För att undvika detta kan man använda optiska mätmetoder. Detta kandidatarbete syftar till studera tre olika metoder för att mäta MMG men även syresättningen i muskler med hjälp av en laser och optiska fibrer. Initial tester genomfördes på stämgafflar då de har en väldefinierad frekvens och vibrerar likt en muskel. Riktiga MMG-mätningen genomfördes på biceps.

Den första metoden bestod av en interferometer som är en vanlig metod för att mäta små vibrationer. Analys och experiment av denna uppställning visade att vibrationer med en amplitud som är större än 300 nm blir mycket svåra att analysera. Givetvis är MMG-signler av betydligt större magnitud och därför bedömdes denna metod olämplig. En betydligt enklare metod innebar att studerar styrkan på ljuset som reflekteras från en vibrerande yta, exempelvis en muskel. Genom att kalibrera mätutrustningen inför mätningen var det möjligt att med stor noggrannhet mäta frekvensen och amplituden hos en stämgaffel på 50 Hz. Mätningar på biceps var inte tillräckligt noggranna för att kunna ge några entydiga resultat och vidare arbete krävs för att utvärdera uppställningen.

I den sista metoden monterades tre optiska fibrer på huden varav två lyste ljus med olika våglängder, färg, och en detekterade ljuset. Tanken bakom detta är att utnyttja det faktum att syrerikt och syrefattigt blod har olika färg, rött och blått. Genom att lysa in i muskeln och mäta hur mycket ljus som togs emot av den tredje fibern kan koncentrationen av syrerikt och syrefattigt blod mätas. Mätning av biceps under kontraktion med denna metod visade hur syremättnaden sjönk till en jämviktsnivå efter cirka 10 s och återgick till balans efter lika lång tid när muskeln fick vila. Genom de mätningar som genomfördes kunde någon MMG signal inte påvisas. Vidare undersökning krävs för att utreda om det är möjligt att mäta både syresättningen och MMG samtidigt. Detta skulle vara till stor fördel för aktiva inom idrottsmedicin.

Slutsatsen som kan dras efter projektet är att frekvens och amplitud hos en stämgaffel kan mätas genom en relativt enkel uppställning som mäter hur ljuset som reflekteras från det oscillerande objektet varierar. Vidare arbete krävs dock för att kunna använda metoden på muskler. Med tre optiska fibrer, varav två som lyser och ett som detekterar, kan syresättningen i muskeln undersökas effektivt. Projektet är första steget i ett potentiellt forskningssammarbete mellan institutionen för fysikalisk kemi och avdelningen för idrottsmedicin vid Potsdams Universitet.

Chapter 1

Introduction

1.1 Optical measurements of mechanomyography

First a brief introduction to the anatomy of muscles will be given, including the concept of motor units. I will then continue by explaining what mechanomyography is and the physical and physiological origin of these signals. Commonly used measurement methods will be reviewed, and our reasons for pursuing a new measurement method will be discussed.

1.1.1 Anatomy of muscles

The muscle that will be studied in this thesis is the biceps brachii which is a skeletal muscles, i.e. the type of muscles connected to movements of the body, see figure 1.1a. The biceps brachii was chosen for several reasons; it is easily accessible, the contraction of the muscle can easily be adjusted, and it has been the subject of numerous studies in the past, (Orizio et al., 1989), (Akataki et al., 2001), (Orizio et al., 2003) and (Beck et al., 2006).

A cross section of a skeletal muscle can be seen in figure 1.1b, showing all the abstraction layers from the whole muscle down to the smallest contractible unit called the myofibril. A collection of muscle fibres connected to one single motor neuron is called a motor unit, as seen in figure 1.1b. When then brain sends a signal to the muscle to contract, an electric pulse is transmitted through the motor neuron. This electrical signal makes the muscle fibres within the same motor unit to contract, but since the signal is an oscillating voltage so is the contraction. This geometrical change of the muscle fibres during the contraction will generate oscillations that will propagate through the tissue out to the surface of the skin (Orizio, 1993). The main goal of this project is to develop an optical measurement technique for these low frequency oscillations on the surface of the skin.

1.1.2 Mechanomyogram

The mechanical oscillations at the surface of the skin created by the lateral oscillation in the muscle has been long known and seen many different names over the years. It was named muscular sound myogram by Orizio et al. (1989) because of their measurement method: a microphone, but as new measurement methods developed the name mechanomyogram (MMG) was initiated by Stokes and Blythe (2001).

The study of mechanomyogram has revealed important information regarding for instance the activation of motor units in the muscle and how this correlates to the force exerted by the muscle and how this can be parametrized by the frequency of the oscillations in the muscle. Barry (1987) studied the mechanomyographic signal from isolated frog muscles which were electrically stimulated. By immersing the muscle in a liquid and placing hydrophones on either side of the muscle, perpendicular to the muscle axis, they could show that the oscillations received by the two hydrophones were phase shifted by $180°$. This proves that the origin of the oscillation must be lateral oscillation of the muscle fibres instead of a radial expansion of the muscle fibres.

Orizio et al. (1996) investigated how the stimulation of individual motor units is expressed in the mechanomyographic signal. By implementing electrodes in the extensor digitorum communis,
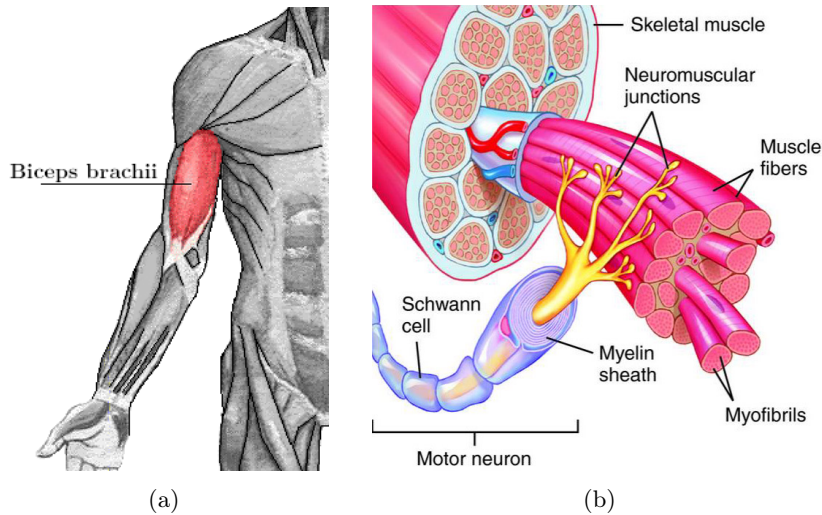
Figure 1.1: (a) Anatomical diagram of the position of the biceps brachii. (b) Anatomical diagram of the motor unit. Image source (Mosby, 2009).

a muscle in the forearm, in man they created two artificial motor units by stimulating two isolated parts of the muscle. To study how the activation of these muscle units express in the mechanomyogram, they stimulated the motor units separately with pulse trains of 3, 8, 9 and 20 Hz. Their results showed that the stimulations of the motor units are summed at the muscle surface in a nonlinear way. This indicates that during voluntary contractions, where the motor units are activated separately, more advanced analysis methods have to be used to deduce the underlying stimulation frequencies of the motor units.

1.1.3 Laser measurements of mechanomyography

Current measurement methods for mechanomyogram usually include piezo electric sensors, as used by Orizio (1993), or accelerometers, Orizio et al. (2003). Both of these measurement methods have proven successful in measuring mechanomyogram, but a possible drawback of using this type of sensors is that they are attached to the skin. Watakabe et al. (2003) studied the reliability of using accelerometers for mechanomyogram and came to the conclusion that a sensor attached to the skin with a weight of more than 6 grams will distort and attenuate the oscillations. To avoid this undesired interference with the signal, several studies during the recent years have utilized different optical displacement sensors, (Orizio et al. (1999), Yoshitake et al. (2008)). The equipment used in these experiments are commercial sensors built to measure displacements by utilizing a system where a laser beam is reflected at an angle from the surface and detected by a sensor. The position of the beam on the sensor is a measure of the displacement of the surface. Measurements by Yoshitake et al. (2008) suggest that the amplitude of oscillations is on the sub millimetre scale, approximately 0.2 mm.

As mentioned before, there have been previous studies doing MMG measurements with lasers but the techniques developed in this thesis have never been tested for this purpose before. Three different measurement methods were proposed: a Michelson interferometer with an oscillating target, a set-up measuring the intensity shift in the light reflected from an oscillating object, and a set-up attempting to measure tissue chromophores and mechanomyogram simultaneously.

Regulations of skin exposure to laser light

To perform laser measurements on muscles, one has to make sure that the laser power is within the limits of maximum permissible exposure for skin (MPE). The recommendations given by The American National Standard for Safe Use of Lasers (LIA, 2007), for the highest power density allowed for skin exposure longer than 10 seconds is presented in table 1.1

Wavelength	W / cm^2
400 - 700 nm	0.2
700 - 1050 nm	$0.2 \cdot 10^{2(\lambda-700)}$

Table 1.1: Maximum Power Exposure for skin for exposures longer than 10 seconds. Source (LIA, 2007)

1.2   Structure of this report

In this report, three different measurement set-ups are proposed. Each will be presented in a separate chapters containing the fundamental theory of the experiment, the method, some results and a concluding discussion about the measurement set-up. Some of the experimental set-ups share some common theoretical background but these will follow each other structurally in the report. In the method step of each experiment, only the fundamental set-up is presented, for a detailed description of the equipment, the reader is referred to the Appendix, section 6.2.

One important part of the data processing in this project is a time series analysis method called the continuous wavelet transform (CWT). Briefly, the CWT is superior to the commonly used fast Fourier transform (FFT) by introducing the time parameter in the analysis, yielding a temporal frequency analysis. As CWT cannot be considered a prerequisite for this thesis, a short review of the CWT is presented in the Appendix, section 6.1.2. The interested reader is strongly recommended to read this part prior to reading chapter 1 and 2 where the CWT is used.

Chapter 2

The Michelson Interferometer

2.1 Introduction

Named after the American physicist and 1907 Nobel laureate Albert Abraham Michelson, the Michelson interferometer is today a fundamental tool for precise measurements of displacements. With an inherent accuracy down to the nano meter scale, we decided to evaluate whether it is suitable for measurements of oscillations on the micro to millimetre scale. To do this we need to derive the theory of this set-up; the theoretical signal received by the detector when performing measurements on an oscillating target, an appropriate method for frequency analysis of the signal and also which limitations this set-up implies. Following this I will present our measurement set-up, the experiments we carried out, the results, and lastly a discussion about the results and the efficacy of this method.

2.2 Theory

2.2.1 Interference in a Michelson interferometer with a oscillating target

The interference between electromagnetic waves in an Michelson interferometer depends on the pathway difference in the two arms of the interferometer created by the beam splitter. The basic configuration of the Michelson interferometer can bee seen in figure 2.1. If one of the arms contains an oscillating object the interference signal must be carefully analysed. To begin this discussion, a basic derivation considering the interference between two electro magnetic waves will be performed and then the oscillation of the object will be introduced.

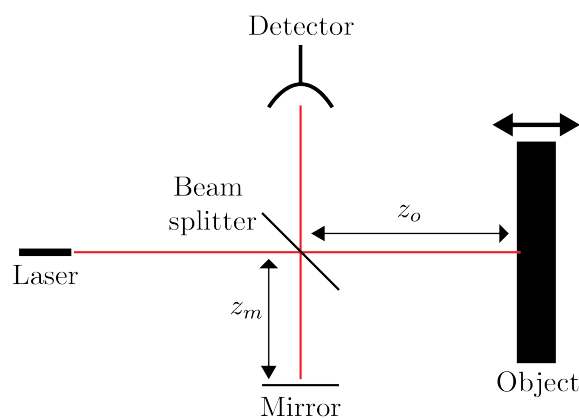The two waves reflected from the mirror and object interfere in the beam splitter where the

Figure 2.1: Schematics of the Michelson interferometer with a moving object.

intensity of the resulting wave will depend on the pathway difference, $z_m - z_o$, between the two arms. The standard equation for the interference of two electromagnetic waves with intensity, I_1 and I_2 (Träger, 2007, eq. 3.211) is

$$I_{1+2} = I_1 + I_2 + 2\sqrt{I_1 I_2}\cos\delta \qquad \delta = \frac{2\pi}{\lambda}(z_m - z_o). \tag{2.1}$$

Since the object is oscillating, i.e. $z_o = z_o(t)$, $2\sqrt{I_1 I_2}\cos(\delta)$ will represent the AC-component of I_{1+2}, which is the signal of interest. Set this AC-component to $m(t)$ representing the message transmitted by the oscillating object, and combine the constants factors to one new variable A_0

$$m(t) = A_0\cos(\delta) = A_0\cos(2\pi/\lambda \cdot [z_m - z_o(t)]). \tag{2.2}$$

To demonstrate how this would work in an experimental set-up, assume a sinusoidal movement of the object with some angular frequency ω and amplitude A_1, this would give

$$m(t) = A_0\cos(2\pi/\lambda \cdot [z_m - A_1\sin(\omega t)]). \tag{2.3}$$

A successful frequency analysis of this signal would yield the oscillation frequency ω and the amplitude A_1 of the object. Depending on the amplitude of the oscillation, A_1, different frequency analysis methods have to be used. Examples of this will be presented in the following derivation. Constructive interference will occur at each point in time when the path way difference between the two arms in the interferometer is equal to half the wavelength of the light, λ,

$$z_m - z_o = \frac{\lambda}{2}. \tag{2.4}$$

If the argument of cos in (2.3) exceeds the domain $[0 : \pi]$ there is an inherent ambiguity in the signal. This would put a restriction on the oscillation not to exceed an amplitude of

$$\frac{2\pi}{\lambda} \cdot A_1 < \frac{\pi}{2} \rightarrow A_1 < \frac{\lambda}{4}. \tag{2.5}$$

As long as the oscillations are within the limits described by (2.5), the intensity of the interference signal is unambiguously correlated to the distance to the object. But as the amplitude increases over the limit, an oscillating interference pattern will emerge. Figure 2.2 shows how this overlap effect translates into a frequency modulation if the amplitude exceeds the limit in (2.5). The conclusion of this is that if oscillations with an amplitude greater than $\lambda/4$ are to be measured, a simple relation between intensity and distance does not exists and a special frequency analysis technique is required.

2.2.2 Movement outside the $[\pi : 0]$ domain

As seen in figure 2.2, a special method for frequency analysis is needed if the amplitude of the oscillation exceeds the limit in (2.5). It appears as if the interference signal is not dependent on the position of the object but rather its speed. If the object is moving with a high speed, it is expected that the signal would oscillate between constructive and destructive interference with a frequency related to the speed of the object. Simulations in the third plot in figure 2.2 show this pattern. It also shows an important aspect of this phenomena: it is not possible to deduce whether the object is moving back or forth, the interference pattern appears to be identical. The property that is observed is instead the speed of the target. The goal of frequency analysis of this signal would be to turn the instantaneous frequency into an amplitude modulation that can easily be analysed. This can be done by utilizing a low-pass filter.

Frequency to amplitude conversion

To convert the varying frequency in the signal in figure 2.2, bottom plot, to an easily measured amplitude variation the following procedure is used. The signal is first passed through a low-pass filter with an appropriate cut off frequency that depends on the amplitude of the oscillation. It is important that most of the frequency content of the interference signal is within the linear regime of the low-pass filter to translate the frequency to amplitude. A filter designed like this would transform a frequency shift to an amplitude modulation. This amplitude modulation will be proportional to the frequency which in turn is proportional to the speed of the object.
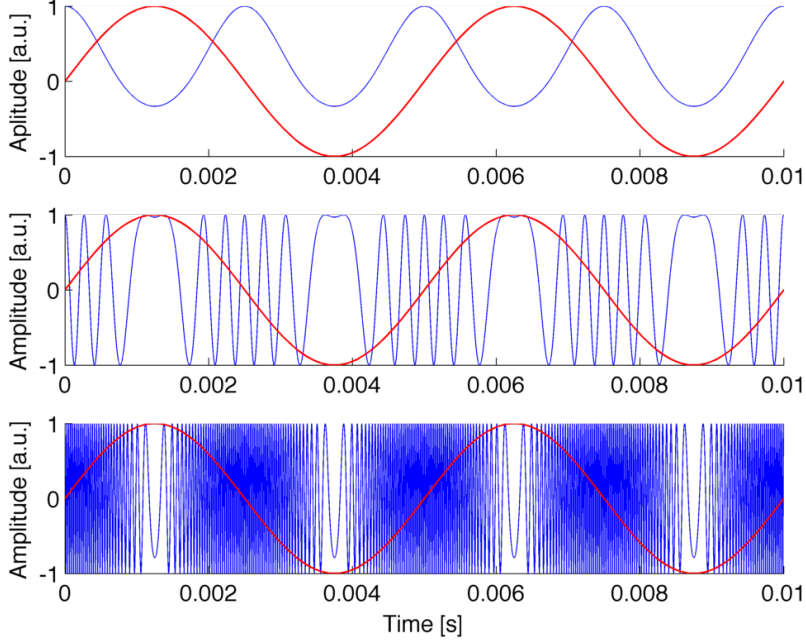
9

Figure 2.2: Comparison of how the amplitude of the oscillation affects the signal. Amplitude of object oscillation: top 10^2 nm, middle 10^3 nm, bottom 10^4 nm. Red curve is the simulated movement of the object measured around its equilibrium point. Blue curve is the interference signal. Simulation done with $\lambda = 685$ nm with an oscillation frequency of 200 Hz.

Calculation of the envelope by a Hilbert transform

The envelope of the amplitude modulated signal can be calculated by means of the Hilbert transform. Consider the arbitrary input signal $m(t)$ seen in figure 2.2, the envelope $e(t)$ can then be calculated through

$$e(t) = \sqrt{y(t)^2 + \mathcal{H}(m(t))^2} \tag{2.6}$$

where $\mathcal{H}$ denotes the Hilbert transform (Pavliček and Michálek, 2012). The red line in figure 2.3a is the envelope, $e(t)$, of the signal, $m(t)$, passed through the low-pass filter. The frequency of this signal is double the oscillation frequency of the object itself, as seen in figure 2.2. Analysis of this signal with the fourier transform yields a plot containing every overtone of the oscillation since the envelop is not a perfect sinusoidal oscillation, see figure 2.3b. The oscillation of the object is half the frequency of the lowest peak in figure 2.3b, which is 400 Hz, i.e. the object is oscillating with 200 Hz. This type of analysis is possible as long as the object is moving with a perfect sinusoidal movement, if this is not the case, non-linear mixing of frequencies will appear which will make the frequency analysis impossible with this method.

2.2.3 Limitations

Bandwidth problems

According to the Nyquist theorem is it only possible to measure time series with a frequency content lower than half the sample frequency. In an experimental set-up with a maximum sampling frequency of f_s the highest measurable frequency is then $f_{max} = f_s/2$. Once again, consider a simple sinusoidal moving object with an amplitude A_1 and an angular frequency ω,

$$z_o(t) = A_1 \sin(\omega t). \tag{2.7}$$

The speed of the object is the first derivative of the displacement $z_o(t)$

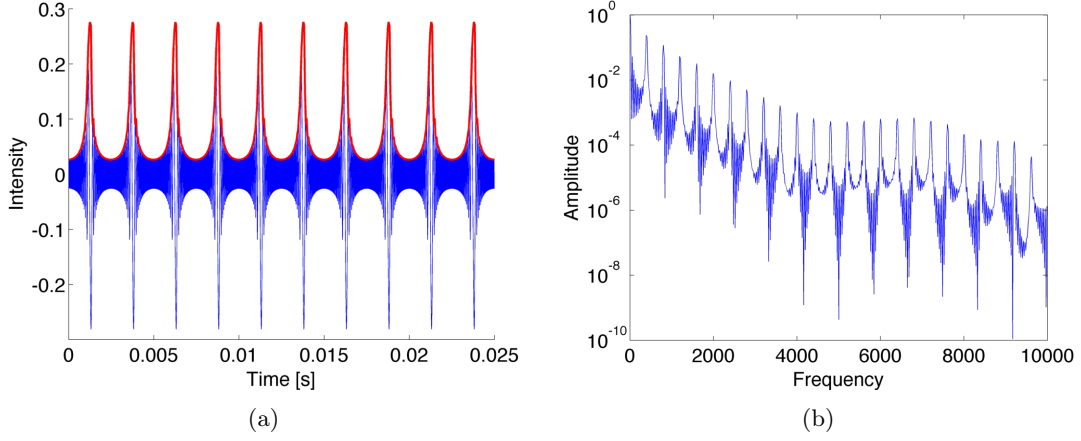$$v_o(t) = z_o'(t) = A_1 \omega \cos(\omega t). \tag{2.8}$$

Figure 2.3: (a) Blue: amplitude modulated signal after processing by the low-pass filter. Red: Envelope calculated by the Hilbert transform. (b) FFT of the envelope signal in (a).

Constructive interference will occur when the relation in (2.4) is satisfied. The frequency at which constructive interference will occur, f_i, is then related to the movement of the object as the following

$$\omega_i = \frac{v_{max}}{\lambda/2} = \frac{2A_1\omega}{\lambda} \rightarrow f_i = \frac{A_1 4\pi f}{\lambda}. \tag{2.9}$$

Consider a case of with an oscillation of 100 Hz with a maximum amplitude of 100 μm and a laser with $\lambda = 658$ nm. This would give

$$f_{if} = \frac{4\pi \cdot 100 \cdot 100 \cdot 10^{-6}}{658 \cdot 10^{-9}} \approx 200 \text{ kHz}. \tag{2.10}$$

This would imply that a sampling frequency of 400 kHz is needed and also that there is no bandwidth limitation in the measurement set-up, e.g. amplifiers.

Non-linear effects of multiple frequencies

If the object is oscillating with a combination of many frequencies and with an amplitude greater than $\lambda/4$ it will be very difficult to deduce these frequencies with the proposed demodulation process. As waves of different frequencies interfere at the detector, non-linear mixing of the waves will occur. In the analysis method described previously, both the low-pass filter and envelope detector are non-linear process that will produce these mixing effects. This can be seen be considering a simple non-linear transformation of a signal consisting of two different frequencies.

Assume a signal $y(t)$ described by

$$y(t) = \sin(\omega_1 t) + \sin(\omega_2 t). \tag{2.11}$$

A simple non-linear process would be to apply the square to this signal,

$$y(t)^2 = (\sin(\omega_1 t) + \sin(\omega_2 t))^2. \tag{2.12}$$

Expanding the parenthesis yiels

$$y(t)^2 = \sin^2(\omega_1 t) + \sin^2(\omega_2 t) + 2\sin(\omega_1 t)\sin(\omega_2 t). \tag{2.13}$$

Using the following trigonometric formulas

$$\sin^2(\omega t) = \frac{1}{2}\left(1 - \cos(2\omega t)\right) \quad \sin(\omega_1 t)\sin(\omega_2 t) = -\frac{1}{2}\left(\cos([\omega_1 - \omega_2]t) - \cos([\omega_1 + \omega_2]t)\right) \tag{2.14}$$

(2.13) can be expanded to

$$y(t)^2 = 1 - \frac{1}{2}\cos(2\omega_2 t) - \frac{1}{2}\cos(2\omega_1 t) - \cos([\omega_1 - \omega_2]t) - \cos([\omega_1 + \omega_2]t). \tag{2.15}$$

This shows how a non-linear process would create many different overtones and mixing frequencies which makes the analysis very difficult.

11

2.3 Method

The Michelson interferometer was set-up according to figure 2.4. (A complete list of the equipment can be found in section 6.2.1.) A 658 nm laser diode was coupled into the interferometer through a 50 μm single mode optical fibre coupled to a collimator. A collimator connected to the detector coupled the light out of the interferometer. The signal from the detector was amplified and then sampled by the data card with a sample rate of 225 kHz to avoid aliasing, as described in section 2.2.3. Frequency analysis of the signal was performed according to the method described in section 2.2.2 by processing the signal with low-pass filter and then apply the fast Fourier transform to the resulting signal. The cut off frequency of the low-pass filter was set to 1000 Hz. The continous wavelet transform was also used to analyze the signal, further described in the results. Due to practical issues this set-up was never used to perform measurements on muscles. Instead a 200 Hz tuning fork was used as an oscillating object.
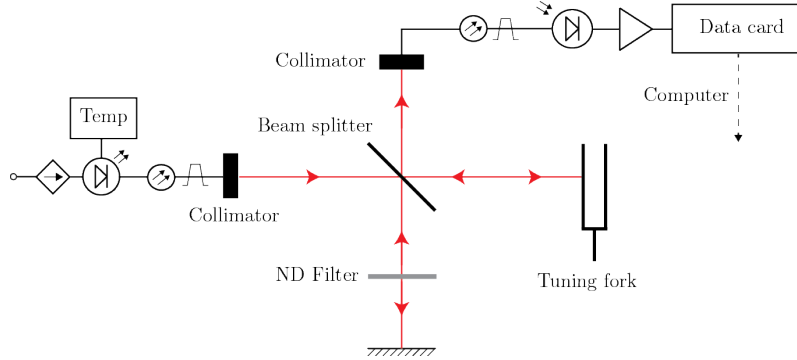

Figure 2.4: Schematics of the measurement set-up.

To get the highest possible contrast in the interference in a Michelson interferometer, the light reflected in both arms of the interferometer should have equal intensity as they interfere. To improve the reflection from the tuning fork, a corner cube reflector film, much like a reflex, was applied to the surface of the tuning fork and measurements with and without it were done to compare the difference. The calibration of the interferometer is described in the following section.

2.3.1 Calibration of the interferometer

When light propagates through the interferometer, it will be attenuated by the beam splitter, the neutral density, ND, filters and the reflection by the tuning fork. These attenuations have been implemented in figure 2.5 using the following annotations

- I_0 - Output intensity from the laser

- α - Attenuation from transmission through the beam splitter

- β - Attenuation from reflection in beam splitter

- ξ - Attenuation from the ND filters

- γ - Attenuation from the reflection of the tuning fork

To get optimal contrast in the interference at the detector the two interfering waves should be of equal intensity, i.e.

$$\frac{\alpha\beta\xi^2 I_0}{\alpha\gamma\beta I_0} = \frac{\xi^2}{\gamma} = 1. \tag{2.16}$$

To get highest possible contrast ND filters was used in the mirror arm of the interferometer to compensate for the high reflectivity of the mirror. A ND filter will attenuate the light transmitted
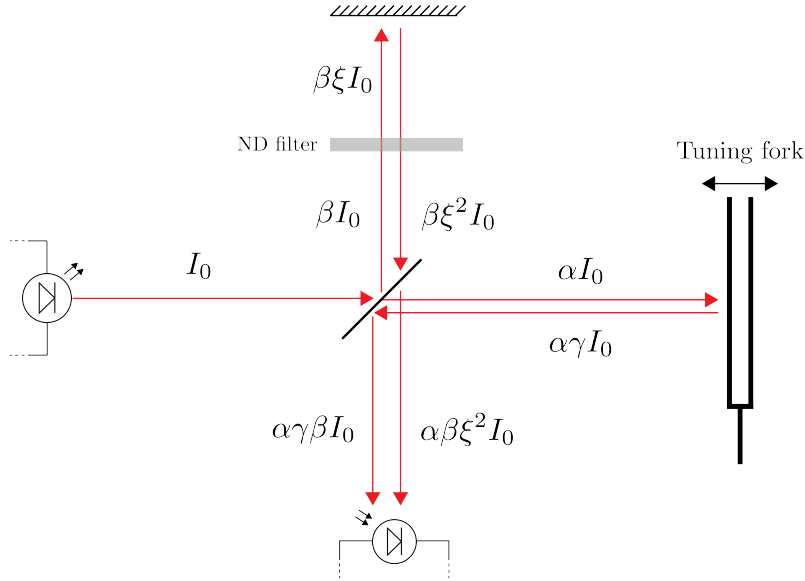
Figure 2.5: The basic set-up of the interferometer.

through the filter exponentially proportional to the optical density, D, of the filter according to the following relation

$$D = -\log_{10} \frac{I}{I_0}. \tag{2.17}$$

Using multiple ND filters result in adding the D values together. The relation between ξ and D is then

$$\xi = 10^{-D}. \tag{2.18}$$

The appropriate value of D can then be calculated with (2.18) and (2.16)

$$\frac{\xi^2}{\gamma} = \frac{(10^{-D})^2}{\gamma} = 1 \Rightarrow D = -\log\left(\sqrt{\gamma}\right). \tag{2.19}$$

To experimentally find the right value of D, the beam power was measured at the following places; in front of the input collimator, after beam splitter to the mirror, and after beam splitter to the tuning fork. The power at each position was measured with a portable power meter and noted, using the corner cube reflector on the tuning fork. The results can be seen in table table 2.1.

Source	Power [mW]
From laser fibre	0.290
Beamsplitter to mirror	0.155
Beamsplitter to fork	0.116

Table 2.1: Beam power at different positions in the interferometer.

When observing the reflection from the corner cube reflector, the bigger part of the signal is reflected back in the same direction. But since the reflector is not a perfect corner cube reflector but instead a film made up from thousands of small corner cube reflectors, there will also be a weak normal reflection from the surface, see figure 2.6. If the reflector is perpendicular to the incoming beam, $\theta = 0$, the reflected beam will be made up from both the corner cube reflection, aI_0, and the normal reflection, bI_0, as noted on figure 2.6. In a non-perpendicular position, $\theta \neq 0$,
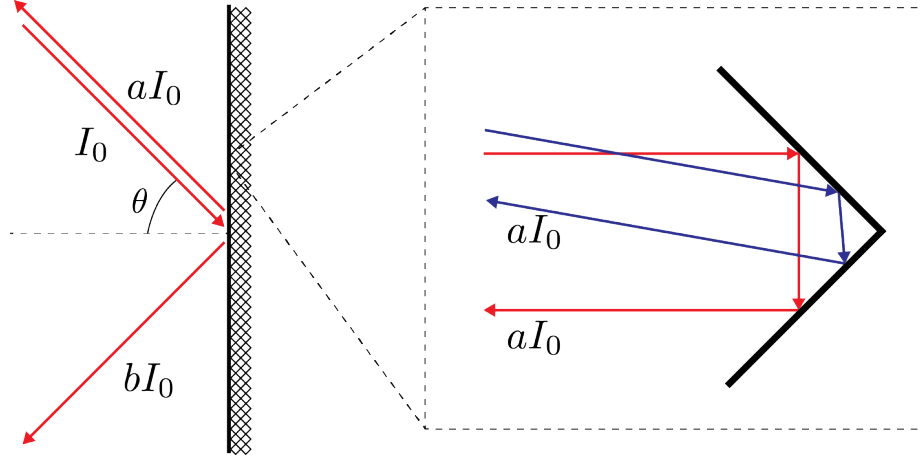
Figure 2.6: Beam propagation with corner cube reflector film. On the right, a magnification of one of the small corner cube reflectors on the film can be seen. This shows the corner cube reflection, aI_0, but since it is a shiny film made up of thousands of these, a normal reflection bI_0 will also exist.

only the corner cube reflection, aI_0, will be reflected back into the interferometer. With an input power to the reflector of 0.116 mW, see table 2.1, the measured power at the detector, with the reflector perpendicular to the beam, and blocking the signal from the mirror, was 0.021 mW. When the reflector was in a non perpendicular position, the signal at the detector was 0.014 mW. So, obviously, the model in figure 2.5 with the constant γ representing the attenuation after reflection from the corner cube reflector needs to be extended to a better model, as described in figure 2.6.

Using the data in table 2.1 the parameters was calculated to

$$\frac{\beta I_0}{I_o} = \frac{0.155}{0.290} = \beta = 0.53, \tag{2.20}$$

$$\frac{\alpha I_0}{I_o} = \frac{0.116}{0.290} = \alpha = 0.4. \tag{2.21}$$

As mentioned, γ needs to be replaced by a and b,

$$a = \frac{0.014}{0.116} = 0.12, \quad b = \frac{0.021 - 0.014}{0.116} = 0.06. \tag{2.22}$$

With a and b, γ, depending on the incident angle θ, can be expressed as

$$\gamma = \begin{cases} a + b & \text{if } \theta = 0° \\ a & \text{if } \theta \neq 0° \end{cases} \tag{2.23}$$

$$\xi = 10^{-d} \tag{2.24}$$

Using these parameters and assuming that $\gamma = a$, D is calculated to

$$D = -\log \sqrt{\gamma} = 0.46. \tag{2.25}$$

The interferometer was therefore adjusted with a combination of ND-filters to achieve this attenuation in the mirror arm. An identical adjustment was done for the tuning fork without the corner cube reflector and instead using a piece of white tape.

2.4 Results

The interference signal from the tuning fork with white tape as reflector is plotted in figure 2.7 and with the corner cube reflector in figure 2.8. Frequency analysis using a low-pass filter and FFT of the tuning fork with white tape is plotted in 2.9a and with corner cube reflector in figure 2.9b.

Further frequency analysis of the measurement was done by using the continuous wavelet transform (CWT). While the FFT only gives information about the total frequency content, the CWT also provides temporal information about the frequency content of the signal. This is particularly important for non-stationary processes such as the contraction of a muscle. Section 6.1.2 in the Appendix provides a brief review of the CWT. Figure 2.10 shows the CWT for the high frequency range, 20 to 90 kHz, while 2.11 shows the CWT for the lower frequency range, 100 to 500 Hz.
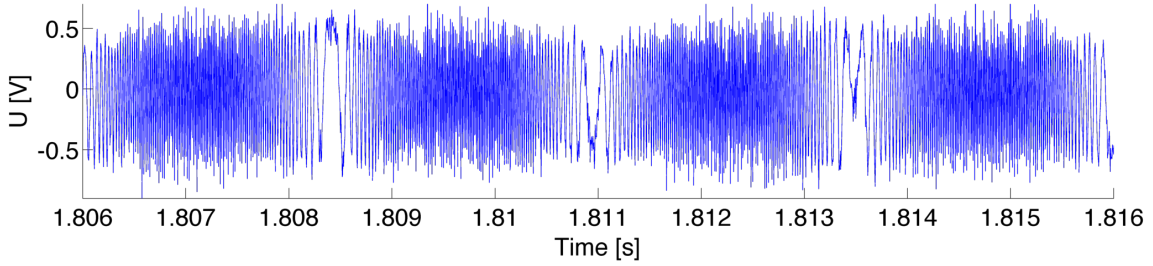

Figure 2.7: Extract of the waveform from measurement of tuning fork with white tape.
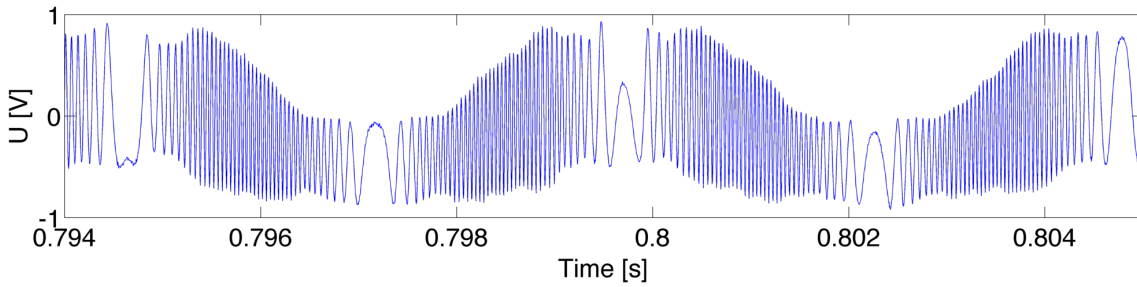
Figure 2.8: Extract of the waveform from measurement of tuning fork with corner reflector.
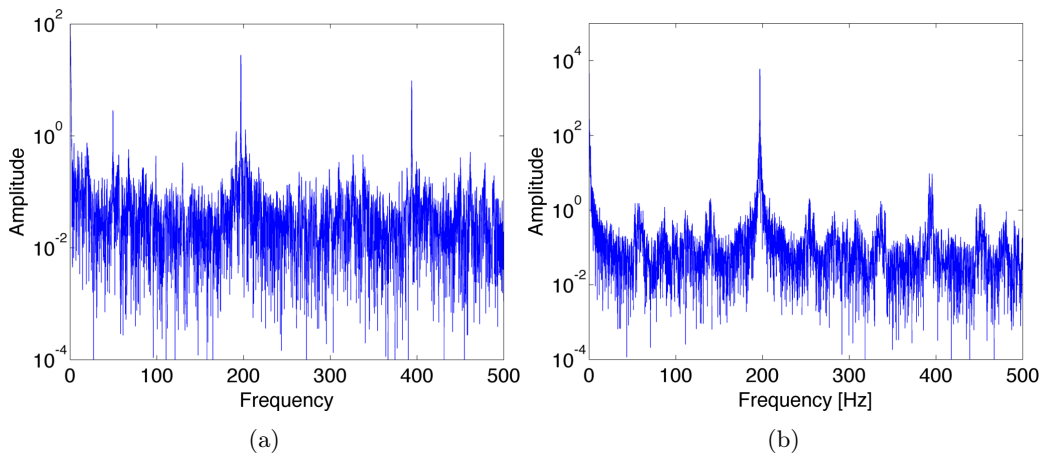
Figure 2.9: FFT of the interferometer signals with the white tape (a) and the corner cube reflector film (b) as reflecting surfaces.

Figure 2.10: CWT of 200 Hz tuning fork. (a) White tape as reflector, frequency range 55 to 90 kHz. (b) Corner cube film as reflector, frequency range 20 - 30 kHz.

Figure 2.11: CWT of 200 Hz tuning fork. (a) White tape as reflector and (b) corner cube film as reflector. Frequency range 100 to 500 Hz.

2.5 Discussion of results

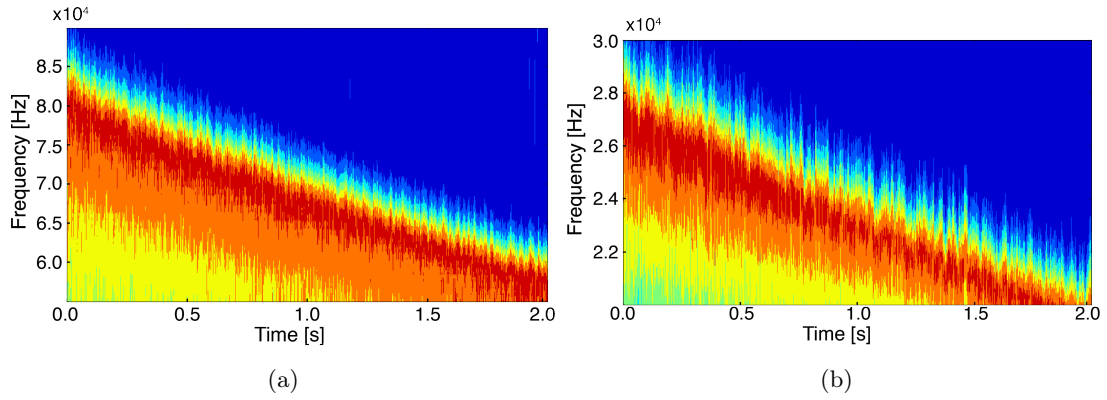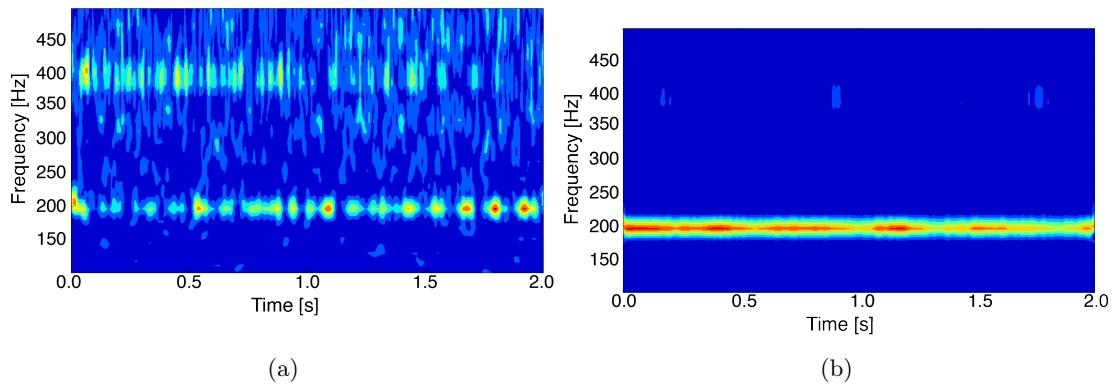The similarity to the simulated signal is apparent in measurement with white tape as reflector, see figure 2.7 and compare to 2.2, while the measurement with the corner cube reflector, see figure 2.8, exhibits a strong amplitude modulation. This is because the corner cube reflector does not reflect all light back in the incident angle, but one part reflects in a normal reflection, see figure 2.6. The white tape has probably a much more diffuse reflection which becomes apparent since the tuning fork does not move in a perfect horizontal oscillation but in an angle. Some fraction of the light could then be coupled out of the interferometer at the end points and introduce an amplitude modulation in the interferometer, see figure 2.12. It is obvious that the amplitude modulation in figure 2.8 arise from the tuning fork displacement since the frequency is half of the interference pattern, as expected with movements outside the $[0 : \pi]$ domain, discussed in section 2.2.2.
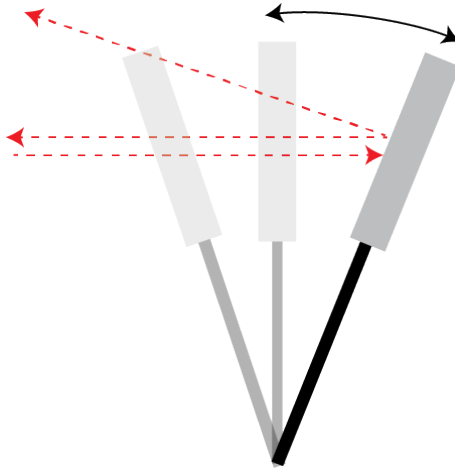

Figure 2.12: Angular movement of the tuning fork and reflection of incident light at the end point.

Frequency analysis of the signals using a low-pass filter and the fast fourier transform differed between the white tape and the corner cube reflector. The 200 Hz peak is almost a factor 100 higher in intensity than the 400 Hz peak for the corner cube reflector. This is due to the heavy amplitude modulation of 200 Hz. The interference signal, which was the goal to measure, is at 400 Hz, double the oscillation frequency. The difference between the 200 and 400 Hz peak is smaller in the measurement with the white tape, since, as discussed earlier, the reflection is more diffuse and less affected by the angular oscillation described in figure 2.12.

The CWT analysis of the signal in the high frequency regime, figure 2.10, illustrates how the highest frequency in the signal is decaying in time. As described in section 2.2.3, the frequency of the interference pattern is proportional to the amplitude of the oscillation of the object. The decaying maximum frequency is therefore a direct measure of how the amplitude of the tuning fork is decaying in time, as expected.

While the high frequency content of the signal yields information about the amplitude, analysis in the lower frequency regime gives information of the oscillation frequency of the object. As noted section 2.2.2, the interference pattern should oscillate with twice the frequency of the object itself. Figure 2.11 shows how the 200 Hz component for the corner cube reflector is very pronounced and barley no trace of the 400 Hz component is present. When the white tape was used as a reflector on the other hand, the signal was not as smooth as with the corner cube reflector. The small islands appearing in the 200 and 400 Hz component indicates that the frequencies are not always present for some reason. This indicates that the measurement was more noisy and the signal was not as stable as with the corner cube reflector.

2.6 Conclusions

The goal of this experiment was to measure a signal of 400 Hz since the tuning fork had a oscillation frequency of 200 Hz. This was thoroughly discussed in section 2.2.2. Unfortunately, the physical phenomena that influence the frequency analysis the most is not the interference pattern but instead an amplitude modulation generated by the movement of the tuning fork of 200 Hz. This is apparent in figure 2.9 and 2.11.

Even though the Michelson interferometer posses the potential of measuring displacements down to the sub micrometer scale, it is not the best solution for oscillations up to and greater than 100 μm. The measurements showed that the interference pattern generated by the oscillating tuning fork was difficult to measure and that the amplitude modulation of the signal had higher impact on the results. This observation suggested that a set-up which focus solely on the phenomena of varying intensity with the oscillation would be more suitable. Furthermore, it was noticed that the set-up required very sensitive adjustments, thus making it a less preferable candidate for clinical situations.

Chapter 3

The intensity shift set-up

3.1 Introduction

When electromagnetic waves are transmitted and reflected at a surface, the intensity reflected back to the source is dependent on the distance to the reflecting surface as well as to the material properties of the reflector. In this experiment a configuration consisting of two optical fibres, one emitting and one detecting light will be presented. The emission fibre illuminates an oscillating surface which reflects the light back to the detection fibre. The intensity of the reflected light is proportional to the distance, and the frequency of the oscillating object can then be achieved through a time series analysis of the detected signal.

In this chapter I will present the theory used in this experiment, the experimental set-up, the results and finally a discussion about the results with a conclusion about the efficacy of this experiment.

3.2 Theory

3.2.1 Amplitude modulation and product demodulation

When performing laser measurements in a setting with ambient light, the laser light can be amplitude modulated to reduce the influence of the ambient light. Set the distance to the oscillating reflecting surface to $d(t)$, and the modulation frequency to ω_m. The signal received by the detector will then be of the form

$$I_D(t) = f\left(d(t)\right) \cdot \sin(\omega_m t) + B \tag{3.1}$$

where f is a function correlated to the reflectivity and scattering properties of the object and the measurement equipment, such as fibres, and B is a constant term including background light. Equation (3.1) also assumes that the response time of the detector is much higher than the oscillation frequency of the object. To extract $d(t)$ from this amplitude modulated signal, the signal is multiplied by the modulation signal $\sin(\omega_m t)$

$$I_{D'}(t) = I_D \cdot \sin(\omega_m t) = \left(f\left(d(t)\right) \cdot \sin(\omega_m t) + B\right) \cdot \sin(\omega_m t). \tag{3.2}$$

Using the trigonometric relation

$$\sin^2(t) = \frac{1 - \cos(2t)}{2} \tag{3.3}$$

the demodulated signal $I_{D'}(t)$ can then be expanded to

$$I_{D'}(t) = \frac{f\left(d(t)\right)}{2} - \frac{f\left(d(t)\right) \cdot \sin(2\omega_m t)}{2} + B \cdot \sin(\omega_m t). \tag{3.4}$$

Applying a low-pass filter and thereby removing the high frequency content, the signal $d(t)$ has been successfully extracted.

3.2.2 Intensity to displacement interpolation

The main goal of this measurement is to deduce the frequency and amplitude of the oscillation. The intensity of the signal is dependent on the distance to the object, $d(t)$, but it is obvious that the relation is not linear, see figure 3.1. Therefore some type of correlation between intensity and distance is needed. There are several approaches to this problem; one could build a theoretical model of the reflection on the object where the intensity is translated into a distance through some mathematical formula, or one could perform a calibration from which the measured $f(d(t))$ can be interpolated to yield $d(t)$, the latter will be used in this thesis.
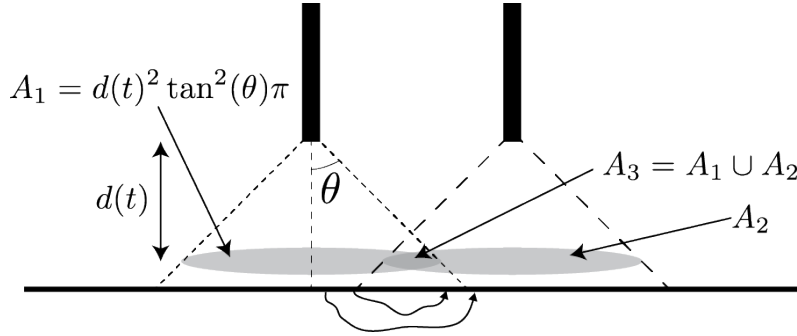

Figure 3.1: The area of the laser beam is dependent on the distance to the object and the numerical aperture of the fibre. The photons received by the detection fibre must either be reflected in the union area A_3, or diffusely scattered through the tissue.

3.3 Method

3.3.1 Measurement set-up

The measurement was set-up according to figure 3.2. (A complete list of the equipment can be found in section 6.2.2.) A laser diode current of 65 mA was set according to the specifications of the laser diode and a modulation signal of 0.5 V and 1 kHz was used to amplitude modulate the laser diode current. A modulation signal with an amplitude of 0.5 V resulted in a laser diode current modulation of 10 mA, this ensures that the current does not drop bellow the laser diode threshold current of 40 mA. The laser diode was coupled into a 600 μm optical fibre to facilitate the measurement procedure. The fibre was mounted in a rubber plug which had two drilled holes, one for the emission fibre and one for the detection fibre. The holes were drilled 4.3 mm apart and ensured that the fibres were mounted steadily and also reduced vibrations of the fibres. The detecting fibre, an identical 600 μm optical fibre, was mounted adjacent to the emission fibre and coupled into a high speed photo diode detector. The amplification level was set to ensure that the amplifier was working in the linear amplification regime as well as to ensure that the input level to the data card did not exceed ± 5 V.

The data card samples the data with a rate of 10 kHz, enough to avoid aliasing effects with a 1 kHz modulation frequency. By also sending the modulation signal to the data card the demodulation was done in Labview according to the product demodulation principle described in section 3.2.1.

3.3.2 Intensity to distance

To correlate the intensity in the measurement to a distance, a calibration measurement was done as described in section 3.2.2. A measurement range was set and within this range, $f(d)$ was measured at 100 points. This region has to be chosen carefully to avoid ambiguities in the measurement. Figure 3.3 shows a calibration measurement done with a 658 nm laser. It is obvious that if measurements are done between 10 and 15 mm away from the object, there is an ambiguity in
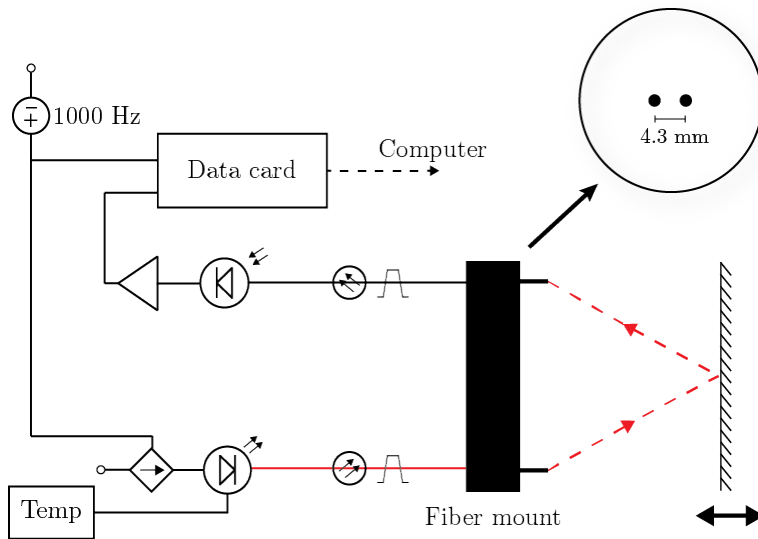
Figure 3.2: Sketch of the intensity shift set-up.

the correlation between intensity and distance. An appropriate measurement range is indicated in figure 3.3. With this measurement range, the object must remain within these boundaries, otherwise the ambiguity mentioned before will also arise. As long as the object remains on the right side of the peak, the correlation is clear. The measured intensity was interpolated to the calibration data through a spline interpolation calculated in LabView.
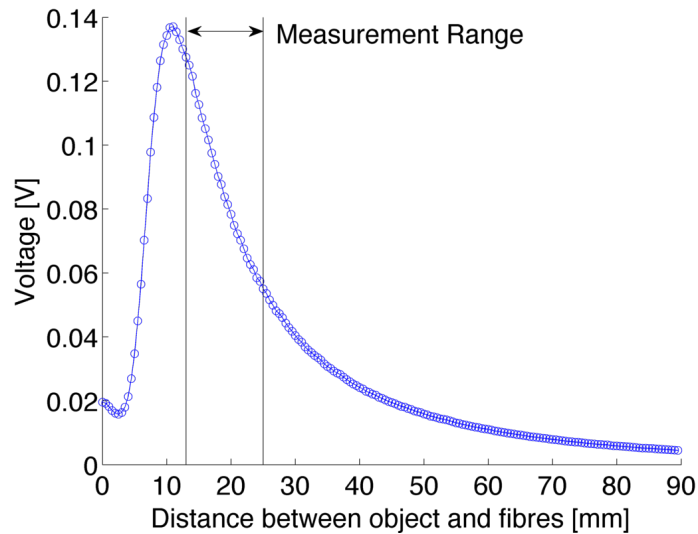
Figure 3.3: A typical calibration curve for the 658 nm laser with the measurement range indicated.

3.3.3   Measurement procedure

The measurements were performed in the following way: the object, tuning fork or muscle (biceps brachii), was mounted perpendicular to the fibres mounted in the rubber plug. The LabView program was initiated and a calibration measurement was performed. The fibre mount was then positioned in the middle of the measurement range where the measurement was performed. Measurements on tuning forks were done by hitting the tuning fork when the measurement started

while the muscle measurements were done by putting a 10 kg weight in the hand of the test subject, see figure 3.4. The arm was positioned in a 90° angle which ensured a large contraction of the biceps brachii.

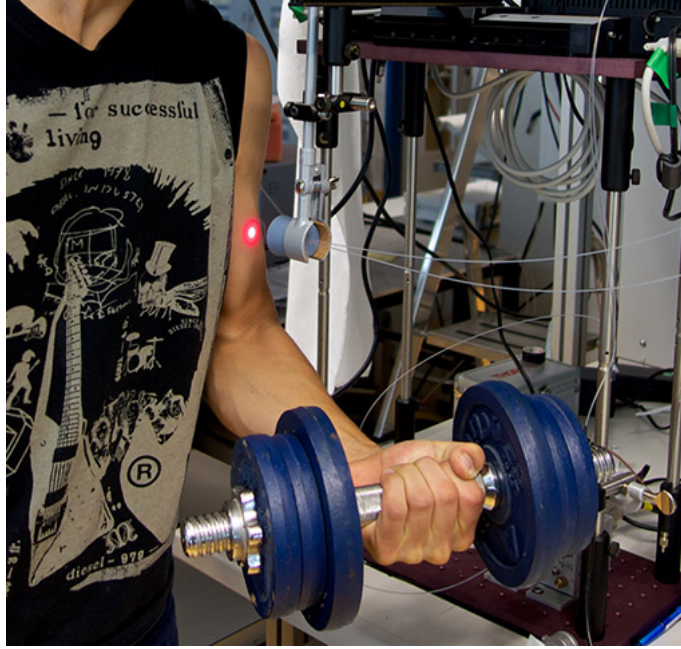Figure 3.4: Example of measurement on the biceps brachii.

3.3.4 Safety

The laser used in the set-up had an output power of 11.5 mW when coupled into a fibre. According to American National Standard for Safe Use of Lasers (LIA, 2007, sec. 3.3), the laser will fall within the classification of **Class 3R**, because of the following parameters:

- The wavelength is within 400 to 700 nm

- The accessible output power is around 11 mW which is more than 5 times the limit for class 2 lasers, 1 mW.

A **Class 3R** laser posses the capability of producing hazardous effects on the eye, and appropriate eye wear should be used at all times. But since the laser light is emitted through an optical fibre, the beam is highly divergent and one has to be very close to be harmed by the laser. With a numerical aperture of 0.37, i.e. a beam cone with 20 degrees spread, the intensity will drop very fast and the dangerous zone is easily avoided. The limits for a laser with wavelength of 658 nm is 0.2 W/cm^2. This limit will set a minimum distance at which measurements can be done to ensure that no harm is done to the skin of the test object. The following formula can be used to calculate the power density, ρ_I, from the fibre with a numerical aperture NA at a distance d,

$$\rho_I = \frac{P_0}{A} = \frac{P_0}{d^2 \tan^2(\theta)\pi} \rightarrow d_{min} = \sqrt{\frac{P_0}{\pi \rho_{Imax}}} \cdot \frac{1}{\tan(\theta)} \tag{3.5}$$

$$NA = \sin(\theta) \tag{3.6}$$

where P_0 is the power at the tip of the emitting fibre, A is the area of the beam at a distance d, and ρ_{Imax} is the power density. Using the parameters given in the experiment yields

$$d_{min} = \sqrt{\frac{11.5 \cdot 10^{-3}}{\pi \cdot 0.2}} \cdot \frac{1}{\tan(20°)} \approx 0.5 \text{ cm.} \tag{3.7}$$

Therefore, according to (3.7), if measurements are done at a distance of more than 5 mm from the skin, it can be considered safe for the test subject. This is no problem since the appropriate measurement range is between 15 and 35 mm from the skin according to figure 3.3.

3.4 Results

Frequency analysis of the measurement was done by using the FFT and CWT, as mentioned in chapter 2.4 and further described in appendix section 6.1.2. Measurements with the intensity shift set-up were done on both a 50 Hz tuning fork and the bicep brachii. Signal plot of the 50 Hz tuning fork can be seen in figure 3.5, and the corresponding frequency analysis in figure 3.6. The CWT of a measurement of the biceps brachii can be seen in figure 3.7 and a summed histogram of the mean power frequency for 5 consecutive measurements on the biceps bracchi can be seen in figure 3.8
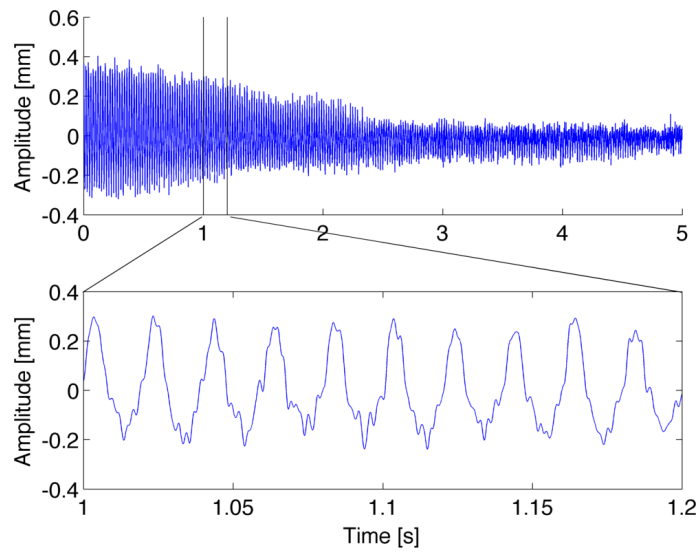
Figure 3.5: A more detailed view of the oscillating tuning fork. The bottom plot show the waveform of the tuning fork clearly.

(a)
(b)

Figure 3.6: Frequency analysis of a 50 Hz tuning fork with a decaying amplitude. Analysed using (a) CWT and (b) FFT

Figure 3.7: CWT of a measurement of the biceps brachii during contraction

Figure 3.8: Summed histogram of the mean power frequency of 5 consecutive MMG measurements of the bicsps bracchi.
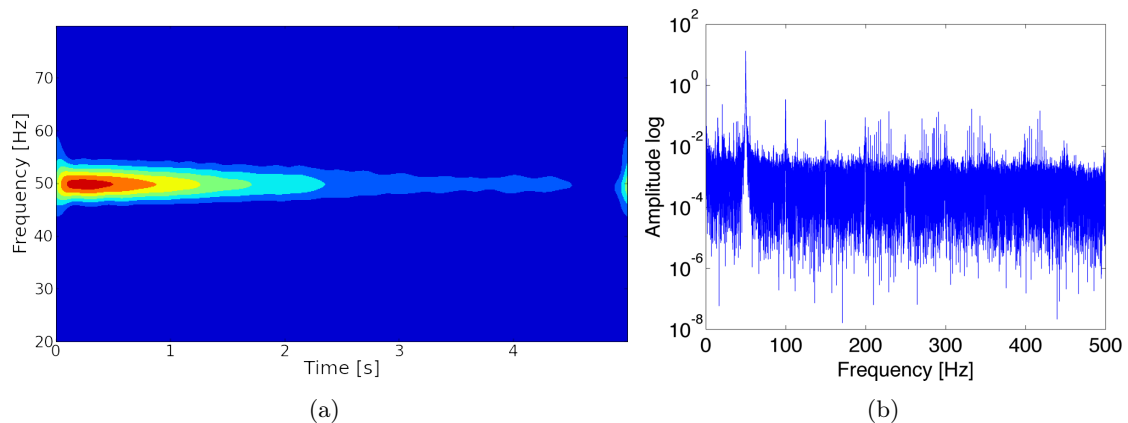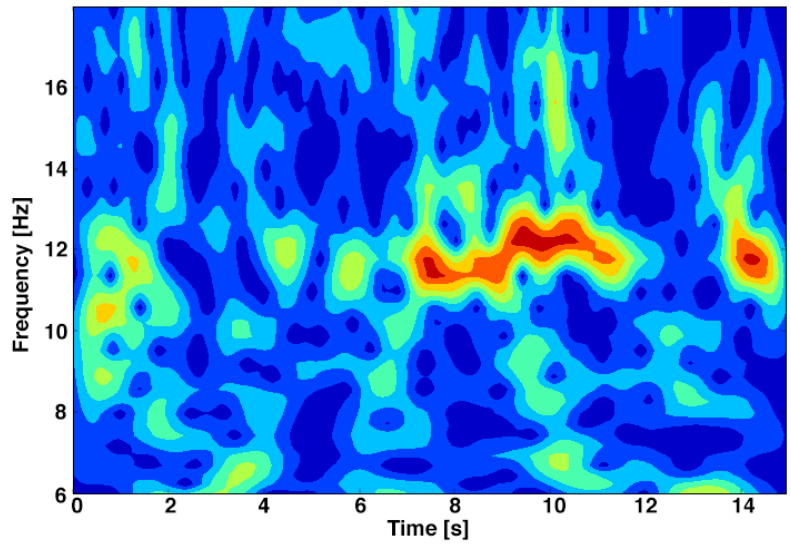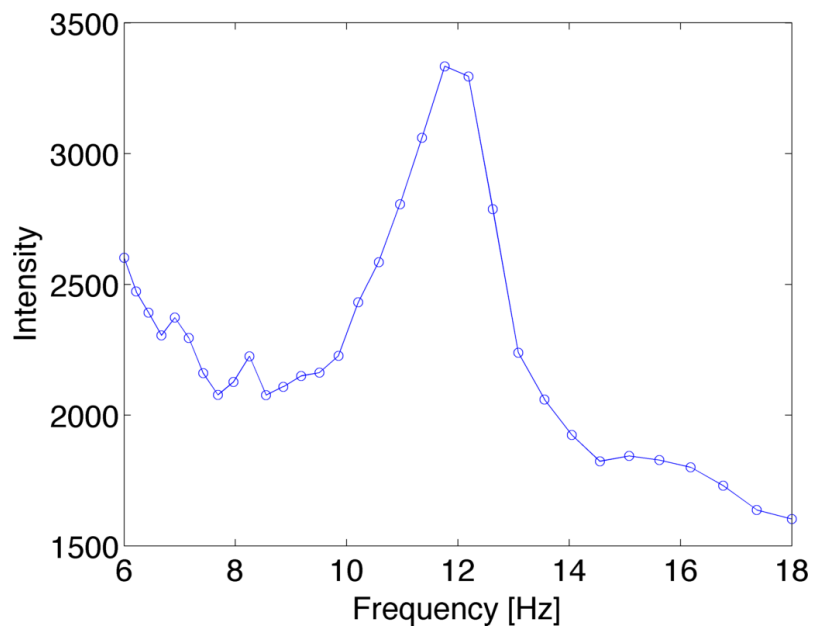
3.5 Discussion of results

The frequency analysis in figure 3.6 shows that the 50 Hz oscillation of the tuning fork is very pronounced in the measurement. Overtones are apparent in figure FFT and are probably produced by non-linear effects in the measurement equipment rather than the overtones of the tuning fork it self since they have very low intensity. The waveform in figure 3.5 shows the movement of the tuning fork on a millimetre scale. The maximum amplitude appears to be about 0.6 mm, decaying to 0 in about 3 seconds. In addition to the decaying signal there is a residual noise signal with an amplitude of about 0.1 mm. This is rather high when the oscillation of interest has an amplitude of 0.6 mm. A specific source for this noise is unknown but the following sources are considered as potential origins:

1. Vibrations in the room due to the air conditioning system

2. Vibrations in the table caused by the fans in the laser controllers

3. Vibrations in the room caused by construction work in rooms underneath the lab

4. Ambient fluorescent light at 100-120 Hz

5. The AD conversion in the data card.

The first two source seems most probable since they would cause continuous vibrations with a specific frequency, which is verified by the FFT in figure 3.6 where several very sharp peaks appear between 200 and 450 Hz. The small width in the frequency domain suggest that these oscillations appear during the complete measurement period, i.e. stationary oscillations. All of the possible mechanical sources of noise presented above and the ambient light can be reduced by performing the measurements on an damped optical table in a dark room.

The CWT in figure 3.6 shows how the amplitude decrease while the frequency of the tuning fork remains constant. The tuning fork is a typical example of a non-stationary process where wavelet analysis is the most suitable method for frequency analysis.

The MMG measurements of the biceps bracchi in figure 3.7 showed no clear oscillation frequency. The darker area between 8 and 12 s around 12 Hz indicates an oscillation but since it is cut off in both ends no conclusions can be drawn. The lack of continuity may be because of movement of the arm. Five consecutive measurements of the biceps brachii was performed and the mean power frequency, MPF, plot of each of these was summed up into a histogram showing the most pronounced frequency common in all the measurements, see figure 3.8. It is clear that the 12 Hz component is commonly apparent in the measurements.

In a study by Akataki et al. (2001) the MPF of the MMG signal in the biceps brachii was found to span from 15 to 40 Hz, depending on the load on the muscle. This may indicate that the 12 Hz component in fact is not the MMG signal, or that that measurement parameters in our experiment differ from those of (Akataki et al., 2001). One crucial factor is the load; Akataki defined the load as a percentage of the maximum voluntary contraction, MVC. At 10% MVC, the MPF was around 15 Hz, a signal around 12 Hz would indicate a load lower than 10% MVC which seems reasonable since the measurements were done with a 5 kg weight for about 15 seconds. The test subject was a young well trained male with no problem carrying the weight for a long time.

3.6 Conclusions

The intensity shift set-up produces good results with the 50 Hz tuning fork, both amplitude and frequency can be measured correctly. Nevertheless, the signal contains much noise and methods for reducing this must be applied to increase the precision of this measurement method. The benefits of the CWT works is most apparent when comparing with the FFT. While the FFT only gives information about the total frequency content, the CWT yield information about how both the frequency and amplitude of the tuning fork change in time.

The biceps brachii measurements showed no pronounced frequency in the CWT. The signal appeared to be discontinuous in the frequency domain indicating that the measurement procedure was unstable. However, the summed histogram of five consecutive measurements indicated a peak

in the average frequency in all of the measurements around 12 Hz. This would in that case be the MMG signal from a contraction lower than 10% of the MVC. In conclusion, this method requires further research before high efficacy results can be produced.

Chapter 4

Tissue chromophores and mechanomyography

4.1 Introduction

As the final set-up in this thesis, we wanted to measure the mechanomyogram and the oxygenation dynamics of haemoglobin in the muscle at the same time. To do this we propose a measurement set-up similar to the intensity shift but with three optical fibres mounted in contact to the skin, two emitting and one detecting light. The hypothesis behind this idea is that as the muscle vibrates, there will be structural variations in the tissue which should result in an oscillation in intensity detected by the detection fibre. The measurement of the oxygenation of haemoglobin in the muscle on the other hand utilize the fact that oxygenated and deoxygenated haemoglobin, HbO_2 and Hb, have different extinction spectra (Prahl, 23/10/2013), see figure 4.1. By using two wavelengths, preferably one around 680 nm and one in the near infra-red, the concentration of HbO_2 and Hb can be measured simultaneously.

In this chapter I will first present the theory behind this experiment including the Beer-Lambert Law and a historical review of tissue chromophores, continuing by explaining our experimental configuration with results and a concluding discussion about the efficacy of this set-up.

4.2 Theory

4.2.1 Tissue chromophores

Measurement of the oxygenation level in the blood was first done by Matthes (1935) and then further developed by Millikan (1942). Millikan, who actually was a doctoral student of Albert Abraham Michelson, the inventor of the Michelson interferometer, developed a device which could be clipped to the ear and measure the arterial blood oxygenation level. He used a broadband light source together with a green and a red filter. The green light, 495-570 nm, was used to determine the thickness of the ear and red light, 620-750 nm, to measure the oxygenation.

When Nick Holonyak developed the first light emitting diode, LED, in 1962 (Holonyak and Bevacqua, 1962) he took the first step in what would come to be a revolution. LEDs are today used in pulse oximetry, a development based on Millikan's device from 1962. A pulse oximeter is a device used to clip on either the finger or the ear to measure the varying absorption, monitoring the pulse and oxygenation level of the arterial blood. Pulse oximeters usually use two LEDs with wavelengths around 660 and 940 nm (Mannheimer, 2007). By using these wavelengths, the device can measure the oxygenation level in the blood as described earlier and visualized in figure 4.1.

Our set-up takes a different approach to this idea where we want to perform the measurements on a muscle and measure the change in oxygenation level during contraction of the muscle. It is expected that the level of oxygenated haemoglobin should decrease as the muscle contracts and the cells use oxygen in the metabolism, while the level of deoxygenated haemoglobin should increase as oxygen is dis-attached from the haemoglobin. An equal change in concentration is expected.
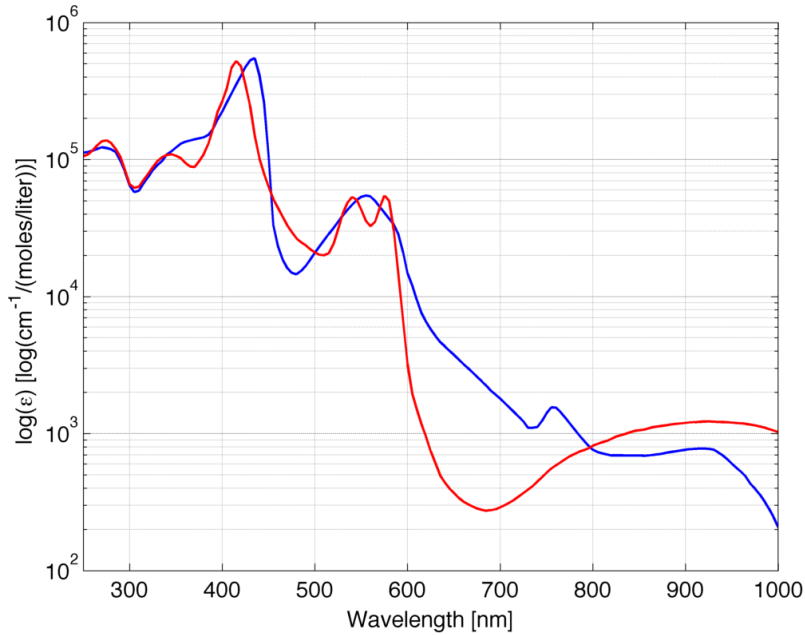
Figure 4.1: Extinction spectra for oxygenated (−) and deoxygenated (−) hemoglobin. Data from Prahl (23/10/2013).

Demodulation of two lasers simultaneously

If a measurement with two lasers and one non-wavelength sensitive detector is to be done, a method for separating the two wavelengths is needed. One possible way of doing this is to amplitude modulate the two lasers with different frequencies, see section 3.2.1 for more about amplitude modulation. The frequencies have to be chosen carefully to avoid interference in the detector. Optical interference is not possible with two different wavelengths but when the detector detects the light, no distinction between wavelengths remains. If there would exist any non-linear processes in the measurement chain, interference between the two frequencies could cause unwanted mixing and overtones.

Consider the case with two lasers with the wavelengths λ_1 and λ_2, modulated with angular frequency ω_1 and ω_2 respectively. The fundamental frequency of the sum of the two modulation frequencies will appear as an interference between the two waves. The fundamental frequency of two frequencies is defined as the greatest common divider between the two, $\mathrm{GCD}(\omega_1, \omega_2)$. If the ratio between the two modulation frequencies is chosen as an irrational number, no common divider exists, assuming infinite precision of the frequencies, and the waves will not exhibit any periodic interference. In reality, frequencies can not be set to a irrational ratio but a reasonable approximation will suffice. The most irrational number one can chose would be $\Phi = (\sqrt{5} + 1)/2$, or as it is more commonly called, the golden ratio.

4.2.2 The Beer-Lambert law

The Beer Lambert law is used to calculate the absorption of light by a substance. The transmission, T, of the light propagation through a material can be calculated through

$$T = \frac{I}{I_0} = 10^{-c\epsilon L} \tag{4.1}$$

where ϵ is the extinction coefficient, c is the concentration of the substance and L is the geometrical propagation length through the substance. The attenuance A of the material can be written as

$$A = -\log_{10}\left(\frac{I}{I_0}\right) = c\epsilon L. \tag{4.2}$$

28

Consider a material consisting of two substances with the concentrations, c_1 and c_2, as well as the corresponding extinction coefficients ϵ_1 and ϵ_2 given in $\mathrm{cm}^{-1}/\,(\mathrm{moles/litre})$. The total attenuance A when an electromagnetic wave propagates through this material can then be written as

$$A(\lambda) = [c_1\epsilon_1(\lambda) + c_2\epsilon_2(\lambda)]\,L \qquad (4.3)$$

where the extinction coefficient ϵ depend on the wavelength of the light λ. To measure both concentrations, c_1 and c_2, simultaneously, two different wavelengths can be used, assuming that the absorption spectra at the two wavelengths differ.

The Beer-Lambert law as stated here is only valid as long as the requirements listed in table 4.1 are satisfied.

Nr	Requirement
1	The absorbers in the medium must act independently of each other
2	The absorbing medium must be homogeneous in the interaction volume
3	The absorbing medium must not scatter the radiation - no turbidity
4	The incident radiation must consist of parallel rays, each traversing the same length in the absorbing medium
5	The substance should be transparent, i.e. low attenuance. Preferably $A < 0.4$

Table 4.1: Requirements for the Beer-Lambert law.

4.2.3 The microscopic Beer-Lambert law

When performing tissue measurements, criterion 2, 3. 4 and 5 in table 4.1 will not be satisfied. Human skin tissue is an opaque, highly scattering medium where the path length of the photons emitted by the source will be much longer than the geometrical distance between the source and the detector, r. This new path length will be denoted $\langle L \rangle$ since it is an average rather than an absolute distance. The relation between $\langle L \rangle$ and r can be written as

$$\langle L \rangle = r \cdot \mathrm{DPF} \qquad (4.4)$$

where DPF is the Differential Path length Factor, as shown by (Johansson, 2007, p.39). The DPF can be calculated by measuring the phase shift of intensity modulated, near-infrared light propagating through tissue (Duncan et al., 1995). Figure 4.2 shows the DPF for a male forearm for four different wavelengths. Using values of DPF from this graph, a fair approximation of the average pathlength, $\langle L \rangle$, can be made. Furthermore, since the scattering effects are wavelength dependent, as seen in figure 4.2, this dependency must be incorporated in $\langle L \rangle$. When the path length L is substituted by $\langle L(\lambda) \rangle$, the regular Beer-Lambert law can be said to be transformed to the microscopic Beer-Lambert law. The validity of this transformation can be seen if one observe short segments of the distance that the photon travels. For sufficiently small distances, the intensity will be attenuated according to the Beer-Lambert Law. The DPF compensates for the scattering effects which cause the photons to travel a greater distance, thus experiencing greater attenuation.

Performing measurements with two wavelengths, λ_1 and λ_2, simultaneously the following system of equations can be formulated

$$\begin{pmatrix} \epsilon_1(\lambda_1) & \epsilon_2(\lambda_1) \\ \epsilon_1(\lambda_2) & \epsilon_2(\lambda_2) \end{pmatrix} \begin{pmatrix} c_1 \\ c_2 \end{pmatrix} = \begin{pmatrix} A(\lambda_1)/\langle L(\lambda_1) \rangle \\ A(\lambda_2)/\langle L(\lambda_2) \rangle \end{pmatrix} \qquad (4.5)$$

By performing an experiment where the intensity at two different wavelengths are measured and then using the microscopic Beer-Lambert law, the concentration of oxy- and deoxy-haemoglobin can be calculated. However, the absolute concentration cannot be calculated. The reasons are twofold; the initial intensity penetrating the surface of the skin I_0 is difficult to deduce, and the pathlength $\langle L(\lambda) \rangle$ is an approximation for the average pathlength. An alternative is to calculate the relative concentration change and choose I_0 as the intensity value at the beginning of the contraction or relaxation and use these values in the microscopic Beer-Lambert law.
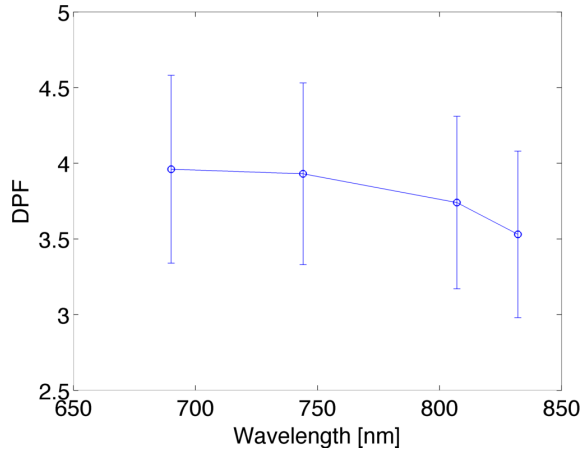
Figure 4.2: DPF calculated for a male forearm, data from Duncan et al. (1995)

4.3 Method

The measurement set-up was setup according to figure 4.3. (A complete list of all the equipment used can be found in section 6.2.3). Each laser diode was connected in the same way as in section
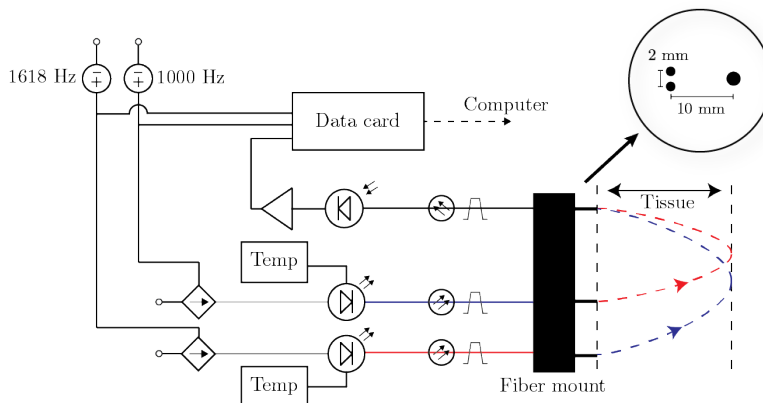

Figure 4.3: Schematics of the tissue chromophores and mechanomyography set-up.

3.3, using a modulation source connected to the laser controller. To avoid interference and mixing in the detector, as mentioned in section 4.2.1, the modulation frequencies were chosen as 1000 Hz and 1618 Hz. The wavelengths of the lasers were 658 nm and 980 nm, with an output power from the fibres of 11.5 mW and 20 mW respectively. The fibres were mounted in a rubber plug according to figure 4.3. The plug with the three fibres was pressed against the skin of the bicep brachii of the test subject. Measurements were done for 30 and 60 seconds, with and without holding a 10 kg weight, hence contracting and relaxing the muscle.

4.4 Results

The first measurement was done for 30 s with an isometric contraction of the biceps brachii, i.e. a constant angle of the elbow, see figure 4.4a. The second measurement was done for 60 s with an isometric contraction between $t = 3$ s and $t = 21$ s and a subsequent relaxation of the muscle, see figure 4.5. The concentrations from these measurement was calculated using the Beer-Lambert law (4.1). I_0 was chosen as the intensity value at the beginning of the contraction / relaxation. To calculate $\langle L \rangle$, r was measured to 1 cm and the DPF for 658 and 980 nm was extrapolated

from figure 4.2 to $DPF_{658} = 4$ and $DPF_{980} = 3.25$. These approximations will yield the relative concentration change. The calculated concentrations are plotted in figure 4.4b and 4.6. The big jumps that appear in connection to the contraction and relaxation of the biceps is due to large geometrical changes of the muscle. As stated in the introduction, the goal was to perform MMG
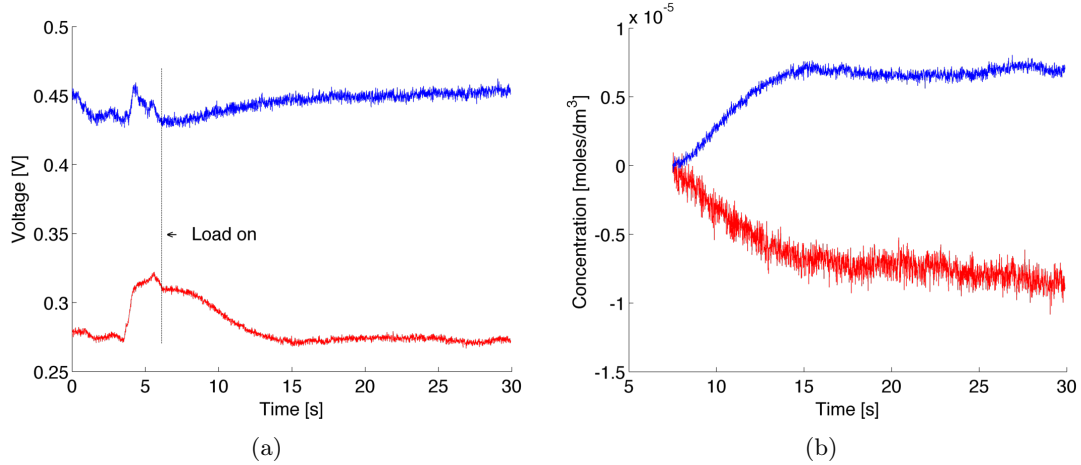

(a)   (b)

Figure 4.4: (a) Intensity signal ($-$ 980 nm, $-$ 658 nm). (b) Relative concentration change of HbO_2 $-$ and Hb $-$ during contraction.
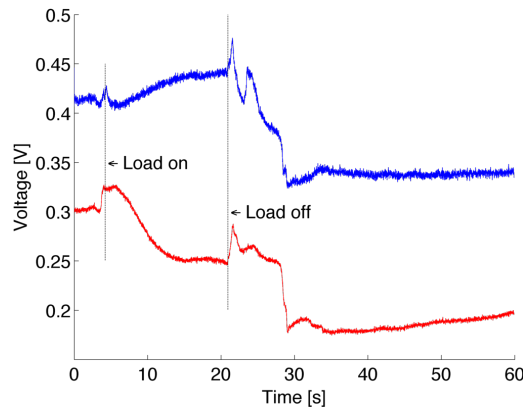

Figure 4.5: Intensity from $-$ 980 nm and $-$ 658 nm. Measurement done for 60 s, contraction of muscle started around $t = 5$ s and ended around $t = 30$ s.

and tissue chromophores measurements simultaneously. To analyse the data for a MMG signal, the CWT was used but no results were obtained. This is most likely due to an error with the amplifier in the set-up. It was noted in the data analysis that a periodic pattern of bursts were appearing on the signal. This would not interfere with the chromophores measurements but the frequency analysis was rendered useless.

4.5   Discussion of results

Even though the main goal of measuring the MMG signal failed, the oxygenation level in the haemoglobin was successfully measured. Figures 4.4 and 4.6 show the oxygenation level of the haemoglobin during contractions and relaxation of the bicep brachii. It is expected that the level of oxygenated haemoglobin will decrease as the contraction progress, consequently the level of de-oxygenated haemoglobin increases by the same fraction. It appears as if the concentration of oxy- and deoxygenated haemoglobin reaches an equilibrium point after about 10 seconds after which
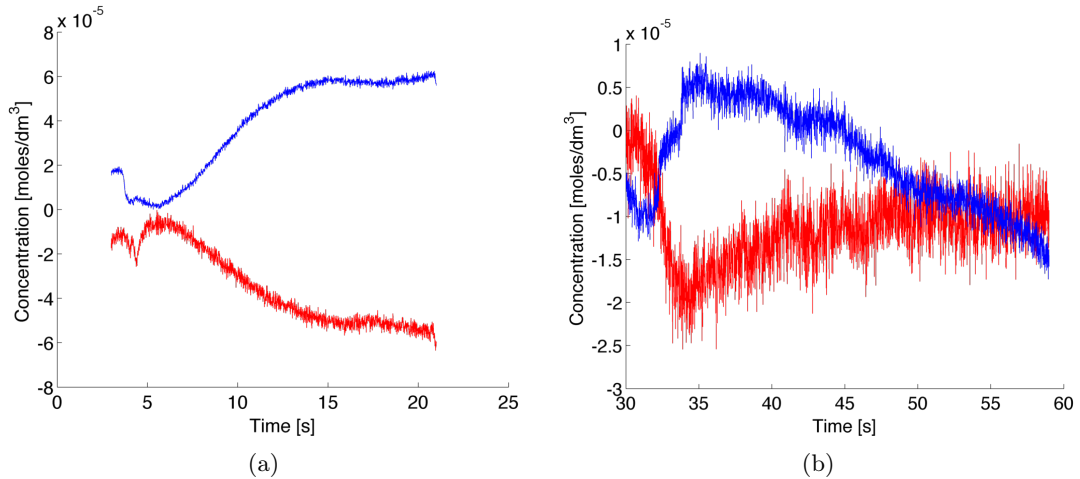
Figure 4.6: Relative concentration change of HbO_2 − and Hb − during contraction, (a), and recovery, (b).

the concentrations remains constant. As expected, the concentrations of HbO_2 and Hb return to their initial states during relaxation.

4.6 Conclusions

The measurement of haemoglobin oxygenation turned out much better than expected. Using dual wavelengths the concentration of oxy- and deoxy-haemoglobin was measured simultaneously. If this could be done together with MMG measurements, it would be a great success and a pathway for more advanced measurements of muscle features. It is still unknown if it is possible to measure the two parameters simultaneously since the amplifier rendered the frequency analysis of the signal useless. If the amplifier had worked as expected, it is still highly unlikely that the measurements would yield any MMG signal since the fibres were pressed very hard to the muscle to couple as much light as possible into the skin. As discussed by Watakabe et al. (2003) a detector with a weight of more than 6 g would interfere with the MMG signal, and the weight equivalent pressure applied on the muscle in our set-up was definitely higher than 6 g. By using a better fibre mount and perhaps some type of gel to reduce the big step in the refractive index, it could be possible to couple more light into the skin without applying such a high pressure. This could be a goal for further development of the technique.

Chapter 5

Summary and Outlook

5.1 Evaluation of measurement configurations

Three different ways for measuring MMG signals were proposed: a Michelson interferometer, an intensity shift set-up and a tissue chromophores / MMG contact measurement. The Michelson interferometer was able to measure very small vibrations but appeared to be unsuited for measurements of higher amplitudes since this would require very high bandwidth in the equipment. Demodulation of the frequency modulated signal appeared to be much harder than expected. Discussions with institute of Mathematics concluded that large amplitude modulations in the signal would complicate the demodulation process significantly. The large amplitude modulations appearing with corner cube reflector showed very were caused by the angular oscillation of the tuning fork. This phenomena turned out to be biggest contributor to the frequency analysis instead of the interference pattern. The frequency analysis also proved to be very difficult if multiple frequencies would be involved. Due to the aforementioned reasons, we decided to develop an experiment solely relying on the phenomena that the reflected intensity depends on the distance to the object.

The intensity shift set-up proved to work as promised when measuring on a 50 Hz tuning fork. The waveform was clearly distinguished and frequency analysis showed a very significant peak at 50 Hz. Measurements of the biceps brachii did not yield any significant MMG frequency from the wavelet analysis, this may be because of unstable measurement set-up with a significant amount of noise.

The third set-up attempt involved a set-up similar to the intensity shift but with three fibres mounted directly on the skin. With two fibres emitting lasers light at 658 and 980 nm, the oxygenation level of the haemoglobin could be measured. It was hypothesised that maybe the MMG signals could also be measured due to the structural changes occurring during muscle contractions. The MMG frequency could not be deduced due to a faulty amplifier that induced noise into the signal, inhibiting a successful frequency analysis.

The conclusion is that the intensity shift set-up posses the ability for measuring the MMG signal but our experimental set-up is flawed in some key aspects. The tissue chromophores measurement is an interesting path to develop further and in combination with MMG measurements this could open up for new ways of studying the human muscles.

Chapter 6

Appendix

6.1 The Continuous Wavelet Transform

6.1.1 Introduction

The Fourier transform is probably the most common way of performing frequency analysis of time series. Implementations of the fast Fourier transform, FFT, provides a time efficient analysis method which is commonly used in scientific software. The FFT is however most suitable for analysis of time-invariant or stationary signals which limits the application areas. When studying MMG signals stationarity cannot always be guaranteed. The process of contracting and then relaxing a muscle would be an example of a non-stationary signal. This problem was considered by Akataki et al. (2001) and Beck et al. (2006) who suggested that the FFT is not an appropriate analysis method for MMG during dynamic muscle contraction since the signal will be non stationary. Akataki instead proposed the use of Short Time Fourier Transform, STFT. The STFT is performed by applying a window function to the signal and the perform a FFT, the window function is then shifted in time and the FFT is performed again. Within the time span of the window function, the signal is assumed to be stationary and that is why the FFT can be applied. A frequency analysis like this yields information about when specific frequency contents appear in the time domain instead of observing the average which the traditional FFT results in.

An alternative method for frequency analysis of non-stationary MMG signals is the continuous wavelet transform, CWT, as suggested by Beck et al. (2006) and Karlsson et al. (2001). Similar to the STFT the CWT provides temporal information about the frequency content in the MMG signal. It is in many ways similar to the STFT with the difference that while the STFT utilize a window function of constant width to gain temporal resolution, the CWT adapts the window size to the frequency. To get a better understanding of the CWT, the next sections will present a mathematical introduction to the continuous wavelet transform, CWT, including some practical examples.

6.1.2 Mathematical formulation of the Continuous Wavelet Transform

The general formulation of the continuous wavelet transform in n dimensions is the following convolution integral (Pathak, 2009)

$$(Wf)(b, a) = a^{-n/2} \int_{\mathbb{R}^n} f(t) \Psi \left(\frac{t-b}{a} \right)^* dt, \quad a > 0, b \in \mathbb{R}^n \tag{6.1}$$

where Wf denotes the continuous wavelet transform of the function f and Ψ is the wavelet. The wavelet used in this project is the complex Morlet wavelet defined as

$$\Psi \left(\frac{t-b}{a} \right) = \frac{1}{\pi^{1/4}} e^{i2\pi f_0 [(t-b)/a]} e^{-\frac{1}{2}[(t-b)/a]^2}. \tag{6.2}$$

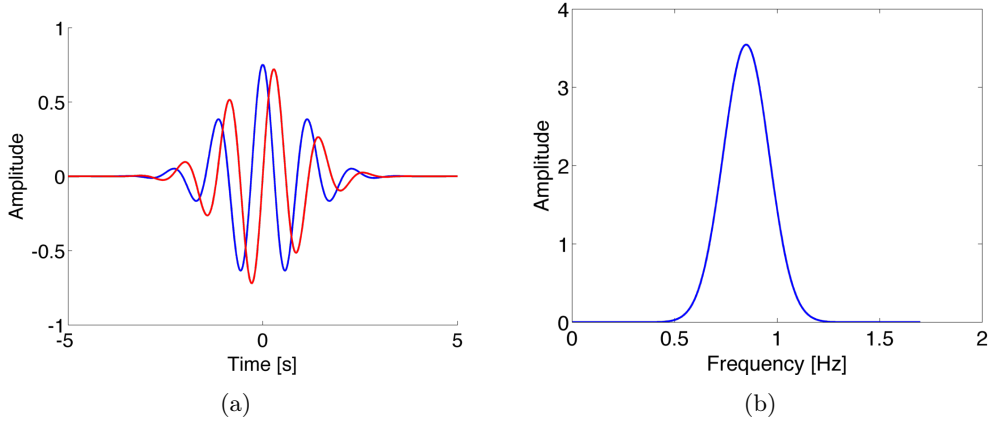The real and imaginary part of the Morlet wavelet are plotted in figure 6.1. This wavelet contains

Figure 6.1: Real $(-)$ and imaginary $(-v)$ part of the Morlet wavelet, (a), and corresponding power spectrum, (b), $f_0 = 0.849$

three important parameters: a, b, and f_0. The parameters a and b appear in the argument of the wavelet and act as a dilation and time shift of the wavelet, exemplified later. f_0 is called the center frequency of the wavelet and is chosen as a fixed value. A value of $f_0 = \sqrt{1/2 \ln(2)}$ is commonly chosen, (Addison, 2002). This choice of f_0 results in a wavelet where the two peaks adjacent to the central peak are half the amplitude of the central peak.

Measurements in this project will only be done in the time domain, therefore (6.1) can be simplified to one dimension as

$$(Wf)(a,b) = \frac{1}{\sqrt{a}} \int_{-\infty}^{\infty} f(t) \Psi \left(\frac{t-b}{a} \right) dt. \tag{6.3}$$

This integral resembles the integral for the Fourier Transform, where $\mathcal{F}$ represents the Fourier transform,

$$\mathcal{F}\{f(t)\} = \hat{f}(\xi) = \int_{-\infty}^{\infty} f(t) e^{-2\pi i t \xi} dt. \tag{6.4}$$

The simple idea behind both Fourier analysis and wavelet transform is to compare an input signal to a another function and see how well they fit. In Fourier analysis, the comparing function is a set of continuous wavefunctions with different frequencies. The integral of the product of the input signal and the wave function is a measure of how well they fit, and easily describes how much of that frequency the input signal contains. The wavelet transform is similar, except that instead of comparing to an infinite wave function, the input signal is compared to a wavelet or wave package. This wavelet is dilated in time to represent different frequencies and shifted in time to analyse every point in time of the input signal.

When the CWT is calculated, the wavelet Ψ is shifted in time, changing b, and dilated, changing a, for all possible combinations. Figure 6.2 shows how the wavelet changes when these parameters are changed. Large values of a dilate the wavelet and shift the frequency content to lower frequencies, and opposite for small values of a. When changing b, the wavelet is shifted left and right in the time domain while the frequency content remains the same. The width of the peaks in the energy spectrum increases by decreasing value of a, i.e. a highly time constrained wavelet will have a large spread in frequency. This can be explained be the rules of Fourier Transform

Consider a signal $f(t)$, the Fourier Transform of the signal is, according to (6.4),

$$\mathcal{F}\{f(t)\} = \int_{-\infty}^{\infty} f(t) e^{-2\pi i t \xi} dt. \tag{6.5}$$

A dilation of $f(t)$ can be written as $f(t/T_0)$, where T_0 is the dilation parameter. The Fourier transform of this signals then reads

$$\mathcal{F}\left[f\left(\frac{t}{T_0} \right) \right] = \int_{-\infty}^{\infty} f\left(\frac{t}{T_0} \right) e^{-2\pi i t \xi} dt. \tag{6.6}$$
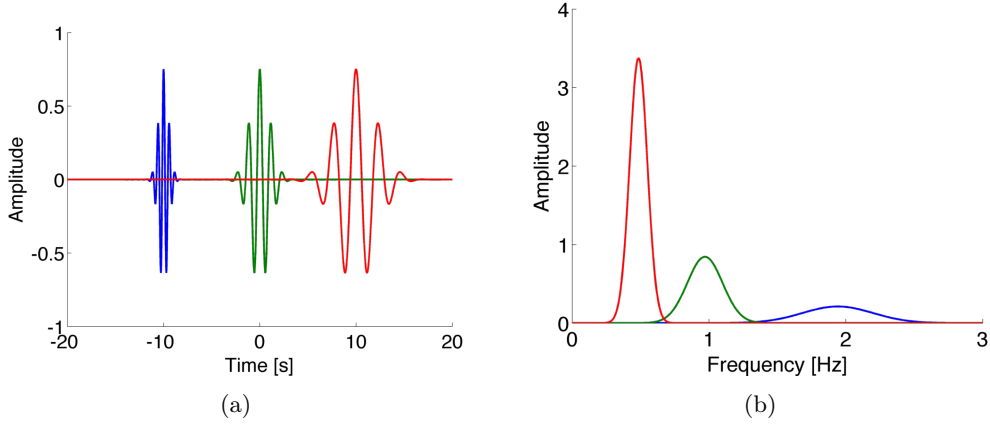
35

Figure 6.2: Real part of three different Morlet wavelets (a), with the corresponding energy spectrum, (b). Blue: $a = 0.5$ $b = -10$, Green: $a = 1$ $b = 0$, Red: $a = 2$ $b = 10$, $f_0 = 0.849$.

Perform the variable change $\tau = \frac{t}{T_0}$ yields

$$\mathcal{F}\left[f\left(\frac{\tau}{T_0}\right)\right] = T_0 \int_{-\infty}^{\infty} f(\tau)e^{-2\pi i T_0 \tau \xi}d\tau \tag{6.7}$$

which implies that

$$\mathcal{F}\left[f\left(\frac{t}{T_0}\right)\right] = T_0 \hat{f}(T_0 \xi). \tag{6.8}$$

This proves why a wavelet that is dilated in time, $T_0 > 0$, has higher amplitude and smaller spread in frequency domain than a compressed wavelet in the time domain with, $T_0 < 0$.

Readers interested in a detailed description of the continous wavelet transform is advised to consult Pathak (2009) for a thorough mathematical derivation or Addison (2002) for an illustrated approach while still keeping a solid mathematical framework.

6.1.3   Examples of continuous wavelet transforms

The best way to get a practical understanding of the CWT is to see some examples. The following examples of the continuous wavelet transform have been calculated using a python implementation of the CWT, developed by Matthias Holschneider and Hannes Matuschek at Potsdam University. Figure 6.3a shows the following signal and its wavelet transform.

$$f(t) = \begin{cases} \sin(2\pi 7t) & 0 < t < 2 \\ \sin(2\pi 20t) & 2 < t < 4 \\ \sin(2\pi 12t) & 4 < t < 6 \\ \sin(2\pi 15t) & 6 < t < 8 \\ \sin(2\pi 10t) & 8 < t < 10 \end{cases} \tag{6.9}$$

A regular Fourier transform of (6.9) would give a frequency spectrum containing the 5 different frequencies in the signal, but no information regarding at what time they appear. One feature of the wavelet transform is that it adds the time parameter and allows for detailed study of how the frequency content in a given signal varies in time. This is clearly shown in figure 6.3b where the CWT displays how the frequency of the signal changes in time very distinctly.

Another example is given in figure 6.4 where the function in (6.10) is plotted with its wavelet transform.

$$f(t) = \sin(2\pi 7t) + \sin(2\pi 20t) + \sin(2\pi 12t) + \sin(2\pi 15t) + \sin(2\pi 10t). \tag{6.10}$$

In this case, the 5 different frequencies are overlayed and therefore appearing all at the same time. This is very clear in the wavelet transform where 5 parallel lines are visible. Both figure 6.3b and
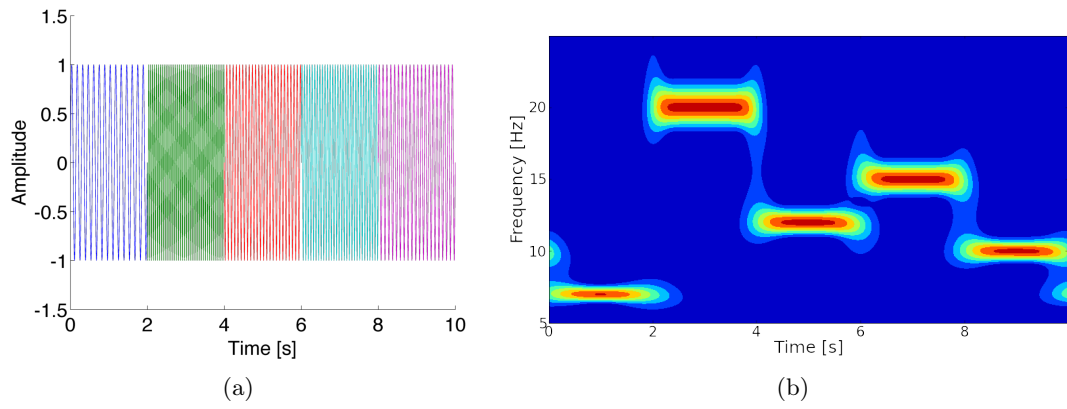
Figure 6.3: Time series (a) and CWT plot (b) for the signal described in (6.9).
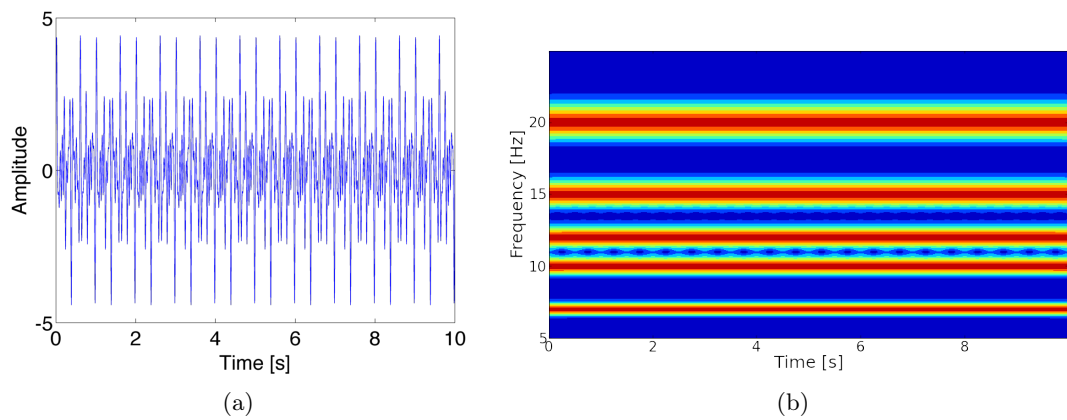

Figure 6.4: Time series (a) and CWT plot (b) for the signal described in (6.10).

37

6.4b show the phenomena described by (6.8); lower frequencies analysed by wider wavelets are tight in the frequency domain, while high frequencies that are analysed by tight wavelets have a big spread in the frequency domain.

To finally show an example of how the wavelet transform can measure how the amplitude of the signal is varying, the signal given by (6.11) is plotted in figure 6.5 with its wavelet transform.

$$f(t) \begin{cases} 0 & 0 < t < 2 \\ t - 2 & 2 < t < 3 \\ \sin(2\pi 10 t) & 3 < t < 6 \\ \sin(2\pi 10 t) \cdot e^{-(t-6)/10} & 6 < t < 10 \end{cases} \tag{6.11}$$

In figure 6.5a the signal is decaying exponentially in amplitude between $6 < t < 10$, this can be
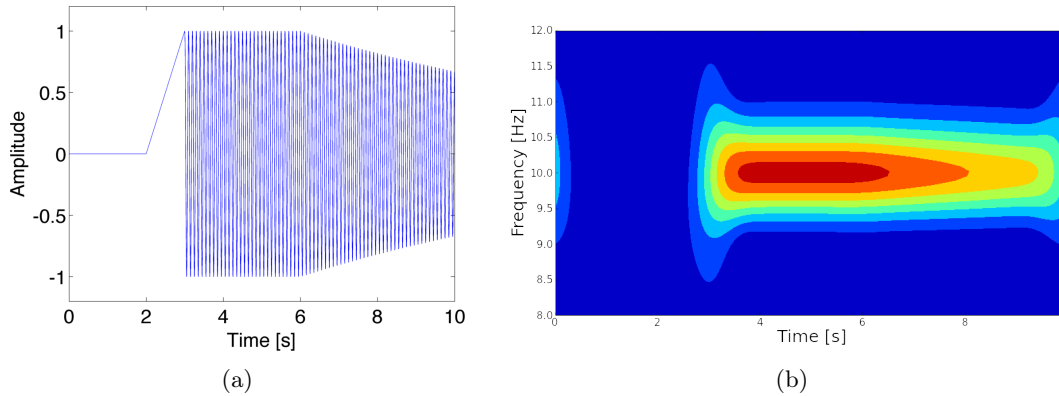

(a)   (b)

Figure 6.5: Time series (a) and CWT plot (b) for the signal described in (6.11).

clearly seen in the wavelet transform plot, see figure 6.5b.

Figure 6.3b and 6.5b show one effect caused by the wavelet script, namely that the script makes the signal periodic by "folding over" a copy of the signal at each end. This is done to reduce boundary effects which otherwise would appear due to the discontinuity at the beginning and end of the signal. In figure 6.3b the tail 10 Hz component is visible in the beginning and the tail of the 7 Hz component is visible at the end as well. The same phenomena is seen in figure 6.5b where the end of the 10 Hz component is visible in the beginning as well.

6.2 List of material
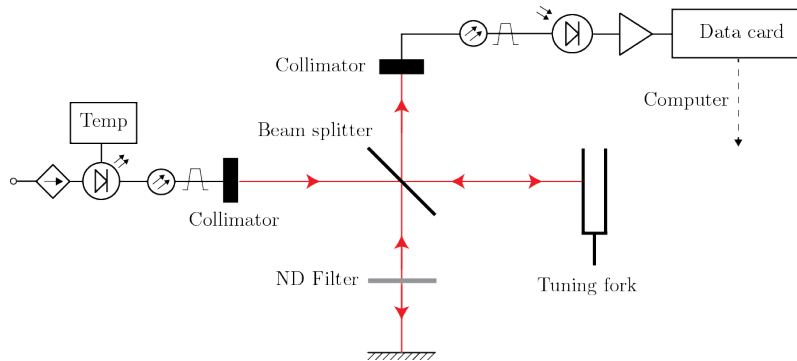
6.2.1 The Michelson Interferometer

Figure 6.6: Sketch of the measurement set-up.

Description	Part Name	Provider
Laser & Temperature Controller	Light Wave LDC 3742C	NewPort
Laser Diode	DL7147-201	Thorlabs
Fibre between diode and collimator	P2-630A-PCSMA-1	Thorlabs
Collimator from laser fibre	F220APC-780	Thorlabs
Beam Splitter	CM1-BP150	Thorlabs
ND Filters	NEK01S	Thorlabs
Mirror	KS1	Thorlabs
200 Hz Tuning Fork		Klangschwingung.de
Collimator to detector	PAF-SMA-7-B	Thorlabs
Fibre, collimator to detector	AFS50125Y	Thorlabs
Detector	DET-110	Thorlabs
Amplifier	DLPCA-200	Laser Components
Data Card	NI USB-6216	National Instruments

Table 6.1: List of equipment used in the interferometer set-up in figure 6.6.
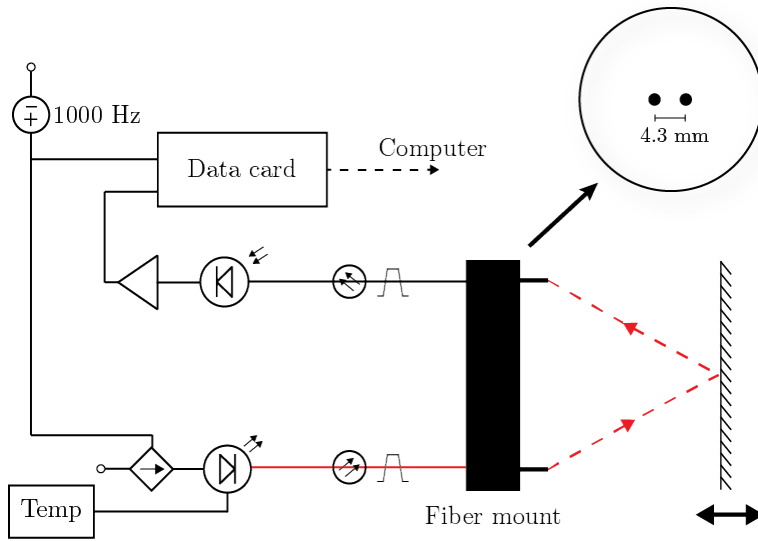
6.2.2 Intensity Shift

Figure 6.7: Sketch of the intensity shift set-up.

Description	Part Name	Provider
Laser & Temperature Controller	Light Wave LDC 3742C	NewPort
Function Generator	AFG 3102	Tektronix
Horizontal Translation Stage	PI M-410 PD	XX
600 μm fibre between laser and fibre mount	JTFLH 600 630 1040	Laser Components
600 μm fibre from fibre mount to detector	JTFLH 600 630 1040	Laser Components
Detector	DET-110	Thorlabs
Amplifier		EG&G
Data card	NI USB-6216	National Instruments

Table 6.2: List of equipment used in the intensity shift set-up in figure 6.7.
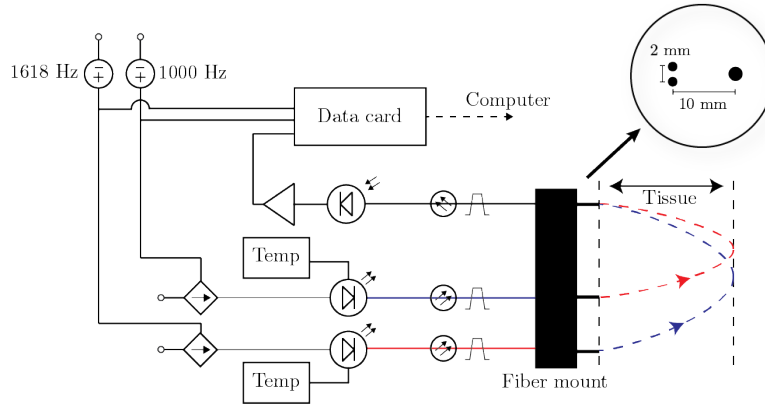
6.2.3 Tissue chromophores and mechanomyography

Figure 6.8: Sketch of the tissue chromophores and mechanomyography set-up.

Description	Part Name	Provider
Laser & Temperature Controller	LDC 3742C	Light Wave by NewPort
Second Temp Controller	ITC-8052	Thorlabs
Second Laser contrl	LDC8040	Thorlabs
Function Gen	AFG 3102	Tektronix
Laser diode 1	DL7147-201	Thorlabs
Laser diode 2	L980P100	Thorlabs
2 x 600 μm fibre from laser to fibre mount	JTFLH 600 630 1040	Laser Components
1000 μm fibre from fibre mount to detector	JTFLH 1000 1035 1400	Laser Components
Detector	DET-110	Thorlabs
Amplifier	DLCPA-200	Femto
Data card	NI USB-6216	National Instruments

Table 6.3: Complete list of equipment used in the tissue chromophores and mechanomyography set-up in figure 6.8.

Bibliography

Paul S Addison. *The Illustrated Wavelet Transform Handbook*. IOP Publishing Ltd, 2002.

K Akataki, K Mita, M Watakabe, and K Itoh. Mechanomyogram and force relationship during voluntary isometric ramp contractions of the biceps brachii muscle. *European journal of applied physiology*, 84(1-2):19–25, 2001.

D Barry. Acoustic signals from frog skeletal muscle. *Biophysical journal*, 51(5):769–773, 1987.

Travis W. Beck, Terry J. Housh, Glen O. Johnson, Joel T. Cramer, Joseph P. Weir, Jared W. Coburn, and Moh H. Malek. Comparison of the fast fourier transform and continuous wavelet transform for examining mechanomyographic frequency versus eccentric torque relationships. *Journal of Neuroscience Methods*, 150(1):59 – 66, 2006.

A Duncan, J Meek, M Clemence, C Elwell, L Tyszczuk, M Cope, and D Delpy. Optical pathlength measurements on adult head, calf and forearm and the head of the newborn infant using phase resolved optical spectroscopy. *Physics in medicine and biology*, 40(2):295–304, 1995.

Nick Holonyak and S Bevacqua. Coherent (visible) light emission from ga (As1- xPx) junctions. *Applied Physics Letters*, 1(4):82–83, 1962.

Ann Johansson. *Spectroscopic Techniques for Photodynamic Therapy Dosimetry*. PhD thesis, Department of Physiscs, Faculty of Engineering LTH, Lund University, 2007.

J.S. Karlsson, B. Gerdle, and M. Akay. Analyzing surface myoelectric signals recorded during isokinetic contractions. *Engineering in Medicine and Biology Magazine, IEEE*, 20(6):97–105, 2001.

LIA. American national standard for safe use of lasers (ansi z136.1—2007). Technical report, Laser Institute of America, 2007.

Paul D. Mannheimer. The light–tissue interaction of pulse oximetry. *Anesthesia & Analgesia*, 105 (6), 2007.

K. Matthes. Untersuchungen über die sauerstoffsättigung des menschlichen arterienblutes. *Naunyn-Schmiedebergs Archiv für experimentelle Pathologie und Pharmakologie*, 179(6):698–711, 1935.

G. A. Millikan. The oximeter, an instrument for measuring continuously the oxygen saturation of arterial blood in man. *Review of Scientific Instruments*, 13(10):434–444, 1942.

Mosby. *Mosby's Dictionary of Medicine, Nursing & Health Professions [With Evolve EBook Package]*. Elsevier Science Health Science Division, 2009. ISBN 9780323065665.

C. Orizio. Muscle sound: bases for the introduction of a mechanomyographic signal in muscle studies. *Crit Rev Biomed Eng*, 21(3):201–243, 1993.

C Orizio, R Perini, and A Veicsteinas. Muscular sound and force relationship during isometric contraction in man. *European journal of applied physiology and occupational physiology*, 58(5): 528–533, 1989.

C Orizio, D Liberati, C Locatelli, D De Grandis, and A Veicsteinas. Surface mechanomyogram reflects muscle fibres twitches summation. *Journal of biomechanics*, 29(4):475–481, 1996.

C Orizio, R Baratta, B Zhou, M Solomonow, and A Veicsteinas. Force and surface mechanomyogram relationship in cat gastrocnemius. *Journal of electromyography and kinesiology : official journal of the International Society of Electrophysiological Kinesiology*, 9(2):131–140, 1999.

Claudio Orizio, Massimiliano Gobbo, Bertrand Diemont, Fabio Esposito, and Arsenio Veicsteinas. The surface mechanomyogram as a tool to describe the influence of fatigue on biceps brachii motor unit activation strategy. historical basis and novel evidence. *European journal of applied physiology*, 90(3-4):326–336, 2003.

Ram Shankar Pathak. *The Wavelet Transform*. Atlantis Press, 2009. ISBN 9491216244.

Pavel Pavliček and Václav Michálek. White-light interferometry—envelope detection by hilbert transform and influence of noise. *Optics and Lasers in Engineering*, 50(8):1063 – 1068, 2012.

Scott Prahl. Optical absorption of hemoglobin, 23/10/2013. URL `http://omlc.ogi.edu/spectra/hemoglobin/index.html`.

M. Stokes and M. Blythe. *Muscle sounds in physiology, sports science and clinical investigation: applications and history of mechanomyography*. Medintel monographs. Medintel, 2001. ISBN 9780954057206.

F. Träger. *Springer Handbook of Lasers and Optics*. Springer handbooks. Springer, 2007.

M Watakabe, K Mita, K Akataki, and K Ito. Reliability of the mechanomyogram detected with an accelerometer during voluntary contractions. *Medical & biological engineering & computing*, 41(2):198–202, 2003.

Yasuhide Yoshitake, Kei Masani, and Minoru Shinohara. Laser-detected lateral muscle displacement is correlated with force fluctuations during voluntary contractions in humans. *Journal of neuroscience methods*, 173(2):271–278, 2008.